Osaka University Knowledge Archive

Title	鉄パラジウム合金のマルテンサイト変態における前駆現象の研究
Author(s)	瀬戸, 秀紀
Citation	大阪大学, 1989, 博士論文
Version Type	VoR
URL	https://hdl.handle.net/11094/925
rights	
Note	

Osaka University Knowledge Archive : OUKA

https://ir.library.osaka-u.ac.jp/

Osaka University

Precursor Phenomena during fcc-fct Martensite Transformation in Fe-Pd Alloys

Hideki SETO

Faculty of Engineering Science
Osaka University

February, 1989

Synopsis

Precise X-ray and neutron diffraction studies have been carried out in the vicinity of fcc-fct transition in Fe-Pd alloys in order to investigate the pretransitional phenomena at martensite transformations. Using a high-resolution X-ray spectrometer with fine temperature control unit, the temperature variation of the profiles of Bragg reflections were measured. A new intermediate phase was discovered in a narrow temperature range between the austenite (fcc) and the martensite (fct) phase. Its structure is characterized by a "two-tetragonal-mixed" phase, and interpreted as a coherent mixture of two tetragonal lattices with different tetragonalities. The origin of the stability of this intermediate phase has been investigated. It is shown that this phase may be interpreted in terms of a "crest-riding-periodon" state proposed by Falk and Barsch and Krumhansl. Temperature variation of Huang diffuse scattering in the cubic phase was also measured. The result was interpreted by a random distribution of tetragonal embryos of the low temperature structure. From these investigations, the process of the first order phase transition in Fe-Pd was inferred by dividing the temperature region into the following four regimes; cubic phase (regime (I)) → random distribution of tetragonal embryos (regime (II)) → two-tetragonal-mixed phase (regime (III)) → tetragonal phase with variants separated by sharp domain boundaries (regime (IV)).

Contents

§1. Introduction 1

A. The process of structural phase transitions 1

B. Precursor phenomena in weakly first order phase transitions 2

C. Martensite transformation of alloys 3

D. The precursors in fcc-fct martensite transformation in Fe-Pd alloy 4

§2. Experimental 7

§2-1. Sample Preparation 7

§2-2. X-ray Diffraction Measurements 9

A. Experimental Details 9

B. Results on the crystals with lower Pd concentrations 10

C. Results on the crystals with higher Pd concentrations 13

§2-3. Neutron Scattering Measurements 16

A. Experimental Details 16

B. Temperature dependence of (200) reflection 16

C. Temperature dependence of the [100]TA phonon 18

§2-4. Huang Scattering 20

§3. Possible Origins of the Intermediate Phase: Crest-riding Periodons 23

§4. Possible Origin of Huang Scattering: Embryonic Fluctuations 32

§5. Conclusion and Discussions 35

A. Conclusion 35

B. Discussions 36

Appendix A 39
Appendix B 42
Acknowledgements 46
References

§1. Introduction

A. The process of structural phase transitions

The mechanism of structural phase transitions in solids has attracted considerable attention in recent years. The phase transition is categorized into the first order transition and the second order transition, and recently the latter has especially attracted investigators' attention. This is mainly because "critical phenomena" are observed at the second order phase transition point.[1] In this case, we can observe the enhanced fluctuations of the order parameter in the critical region which are not easily detected in usual (non-critical) situation. Thus we can obtain information on various aspects of the microscopic properties of solids. In the case of second order phase transition, the thermodynamical potential curve is essentially expressed by a single minimum (see Fig.1-1). At the transition point, the curvature at the minimum becomes zero, which gives rise to large amplitude fluctuations of the order parameter. At the same time, "critical slowing down" of the relaxation time or "critical softening" of phonons of fluctuations take place. These anomalies can be observed by, *e.g.*, neutron scattering experiment.

On the other hand, first order phase transitions have been thought to be less interesting as far as thermal equilibrium state is concerned. In the case of the first order transition, the thermodynamical potential is characterized by double minima (or multi-local minima) corresponding to the high temperature phase and the low

temperature phase (with several variants). The phase transition is caused by the change of absolute minimum as the temperature is varied. (See Fig.1-2.) In this case, there is no critical fluctuations associated with the phase transition. Thus the first order transition is considered to be a simple process.

B. Precursor phenomena in weakly first order phase transitions

In recent years, however, new interesting experimental results observed just above first order phase transitions have been reported. These effects are generally called "precursor phenomena".

Experimental evidences for precursors are; anomalies in transport coefficients,[2,3] diffuse and extraordinary diffraction effects in diffraction experiments,[4,5] a distinctive cross-hatched texture known as "tweed pattern" in the electron microscope image,[6-8] etc. These phenomena have been observed in alloys,[9,10] minerals,[11,12] ceramics,[13] ferroelectrics,[14] Jahn-Teller materials,[15,16] intermetallic compounds,[17-20] etc. It is recognized that 'precursors' exist particularly in weakly first order phase transitions where mode softening does exist but it remains incomplete up to the transition temperature.

It is convenient to divide the temperature region into the following regimes depending on the characteristic of the potential function (see Fig.1-2).

(I) $T_0'<T$: potential has single minimum at ζ_0,

(II) $T_c<T<T_0'$: minima at ζ_0 and $\pm\zeta_1$, $(U(\zeta_0)<U(\pm\zeta_1))$,

(III) $T_0<T<T_c$: minima at ζ_0 and $\pm\zeta_1$, $(U(\zeta_0)>U(\pm\zeta_1))$,

(IV) $T<T_0$: minima at $\pm\zeta_1$.

The precursor phenomena is considered to take place in the temperature regime II and III.

C. Martensite transformation of alloys

Experimentally, precursors in thermoelastic martensite transformation have been investigated extensively. The martensite transformation is characterized by diffusionless displacive phase transition. Among these, 'thermoelastic' type materials undergo weakly first order phase transition and tend to show the shape memory effect. The thermoelastic martensite transformation is further subdivided into two classes; bcc-hcp (and related long period hexagonal layer stacking structures), and fcc-fct transition.

In bcc-based alloys, anomalous X-ray scattering effects were reported as an peculiar precursor effect in Ti-Ni[21,22] and Au-Cd.[23] It has been shown that in these materials the diffuse scattering spots characterizing the low temperature long period structure already appears in the temperature region where the crystal still maintains original cubic symmetry. Not only that, these diffuse spots show peculiar incommensurability. That is, the amount of shift from the commensurate position is dependent on the reference Brillouin zone. This fact is definitely in contradiction to the interpretation of the conventional periodic modulated structure such as CDW state. Yamada[24,25] and co-workers[26,27] showed that such peculiar incommensurability can be explained by "dressed embryo" model.

This model assumes that in the temperature region II or III there are random distribution of locally transformed micro-regions, which are accompanied by strain field around them.

This interpretation seems to give a key for the general understanding of precursor phenomena at first order phase transitions.[28] That is, when a system undergoes first order structural transition, micro-regions (embryos) of the low temperature phase are created with finite density even in thermal equilibrium state where the system still maintains high temperature structure on average. If this is the correct general feature, the first order phase transition associated with a precursor phenomenon may be described in terms of the 'key words' such as embryo density, embryo-embryo interaction, embryo creation energy, embryo life-time, etc.

It is therefore very important to verify experimentally whether similar 'embryo' picture can be established in other systems or not. The most straightforward extension of application will be to fcc-fct martensite transformations.

D. The precursors in fcc-fct martensite transformation in Fe-Pd alloy

$Fe_{1-x}Pd_x$ alloys containing about 30-at% palladium are known to undergo a thermoelastic martensite transformation from fcc to fct,[29] and exhibit the shape memory effect. The martensite transformation temperature (T_m) decreases from about 300K to 0K with increasing palladium concentration within the region of $0.29 \leq x \leq 0.32$. (See Fig.1-3.) This phase transition is weakly first order as is known from

the shape memory effect, small hysteresis and small order of tetragonality just below T_m examined by Sohmura *et al.*[30] Similar to the other shape memory alloys such as In-Sn,[31] Mn-Cu,[32] etc., "tweed micro structure" has been observed.

Sugiyama *et al.*[33,34] found the precursor phenomenon and investigated its temperature variation in detail by using transmission electron microscopy. Upon decreasing temperature from the uniform fcc phase, mottled contrast gradually appear at about T_m+100K, get clearer in contrast to be cross-hatched structure with elongation to [110] directions, and become so-called "tweed pattern". From the observation by an electron diffraction in the same condition as observing tweed pattern, they found diffuse streaks perpendicular to the striations of the tweed, and showed one-to-one correspondence between them. From these results, they concluded that the diffuse streaks are not caused by the thermal diffuse scattering, but are caused by static displacements of atoms.

Further, the neutron scattering study by Sato *et al.*[35] and the measurements of the Young's modulus by Sugiyama *et al.*[36] showed that the softening of the [110] TA_1 phonon mode occurs in the temperature range where the tweed pattern is observed. From these experimental results, Ohshima *et al.*[34] explained the origin of the tweed contrast by the formation of small platelike fct nuclei in the parent austenite phase before the phase transition.

The experimental results and the model of the martensite transformation described by Sugiyama *et al.*[33,34] are in good

agreement with the "dressed embryo" model mentioned in the preceding section.

The purpose of the present investigation is to carry out detailed X-ray and neutron scattering study on Fe-Pd alloy in order to clarify structural and lattice dynamical aspects of the martensite transformation.

§2. Experimental

§2-1. Sample Preparation

Four Fe-Pd alloys nominally containing 30.1, 30.2, 30.8 and 31.2 at%-Pd were prepared. Each ingot was obtained by arc melting of 99.99% iron powder and 99.95 % palladium powder. Single crystals were grown by the Bridgman method in argon atmosphere. They were annealed for four days at 1373K for homogenizing in concentration and quenched in iced water. The as grown crystals contained some small grains with other orientations, which were cut out by carbon blade wheel cutter to have large single crystals suitable for neutron scattering experiment . Fragments were shaped into needles with the long axis along $[001]_{fcc}$ direction to be specimens for X-ray diffraction, and etched by a ferric chloride solution so that the size of these samples became about 0.4 × 0.4 × 7 mm^3. Other fragments were chemically analyzed their palladium concentration by Agne Gijutsu Center, and it became to known that the two samples containing 30.1 and 30.2 at%-Pd were the same as their nominal composition, but another two containing 30.8 and 31.2 at-%Pd were different from their nominal values. In order to determine the homogeneities about the concentration of these crystals, the smearing of the transition temperature were measured by neutron scattering as is described in §2-3. The transition point of the two samples with lower Pd concentration were determined exactly so that they may be believed to be homogeneous in whole the crystals, but of the two with

higher Pd concentration were smeared over a range of 100K so that they may have concentration gradient with about ±1 at%.

§2-2. X-ray Diffraction Measurements

A. Experimental Details

In most of the experiments, a molybdenum target rotating anode X-ray generator (Rigaku RU-200) was used under the condition of 50kV and 60mA with a fine focused filament, and germanium (111) reflection was utilized as a monochromator. The divergence of the incident beam was limited by a 0.2mm wide and 0.7mm high slit system. A position sensitive proportional counter (PSPC) with Xe and CH_4 mixed gas was put in use effectively for our purpose. The length of the sensitive area was 50mm and was divided into 256 channels. Each channel corresponded to 0.026 degree. Since the samples were composed of many mosaic crystals which were slightly larger than the beam size, different grains were irradiated when the crystal was rotated by a large amount. The temperature of the samples were controlled within ±0.02K by a closed-cycle helium refrigeration system (Osaka Sanso Cryo-mini) and a personal computer. The schematic representation of the instruments is depicted in Fig.2-2-1(a).

In some of the experiments (especially for the sample containing 30.2 at%-Pd), a iron target X-ray tube was used under the condition of 40kV and 15mA, PG (pyrolytic graphite) (002) reflection as a monochromator. In these conditions the instrumental resolution was lower than the former one because the beam divergence from the PG monochromator is broader than that from Ge monochromator.

(See Fig.2-2-1(b).)

*B. Results on the crystals with lower Pd concentrations**

A sample containing nominal 30.1 at%-Pd was investigated. We can believe that it contains 30.1 at%-Pd actually from the reason described in §2-1. Its mosaic spread was 0.036 degree at FWHM and its lattice constant was 3.756±0.001Å at room temperature.

Temperature dependence of the line profile of the (600) reflection was precisely investigated. If the transition process is simply described by cubic to tetragonal transition, $(600)_{fcc}$ reflection should decrease and new $(600)_{fct}$ and $(006)_{fct}$ reflections of the tetragonal structure should grow as the temperature is decreased. On the contrary, the observed scattering profile showed a complicated feature within a narrow temperature range just above the "pure tetragonal structure" range: Upon cooling from the cubic phase, new two peaks (peak 2 and peak 3 in Fig.2-2-2) appeared at T=273K ($=T_1$) on a slightly lower angle side of the original $(600)_{fcc}$ peak (peak 1 in Fig. 2-2-2) which shifted to the higher angle side gradually. In this temperature region, these peaks stayed on the original $(001)_{fcc}$ reciprocal lattice plane. Upon further cooling below T=265K ($=T_2$), peak 2 suddenly vanished, while peaks 1 and 3 moved off the (001) reciprocal lattice plane (see Fig. 2-2-3(a)). This result indicates that the sample transformed to the low temperature fct phase at T_2 and the well-known twinned structure with the {110} twin boundary was

* These results were already published in *J. Phys. Soc. Jpn.*[37)]

constructed at the same time. Therefore, it is inferred that there exists a new intermediate state between T_1 and T_2.

The lattice constants corresponding to these peaks are plotted against temperature in Fig. 2-2-3(b). Below T_2, the lattice constants for peaks 1 and 3 are identified, respectively, as the lattice constants a_t and c_t of the tetragonal lattice (a_t=3.795Å, c_t=3.725Å, c_t/a_t=0.982 at 264.8K). In the intermediate temperature region, $T_2<T<T_1$, the difference between the lattice constants for peak 1 and 3 are considerably smaller than that of the fct phase below T_2. Moreover, there is another unidentified lattice constant corresponding to peak 2. All the peaks in this temperature region do not show the broadening in their width (see Fig. 2-2-4). The possibility that there could exist other concentration regions in the irradiated crystal which have different transition temperatures is ruled out because the crystal has a single tetragonal lattice below T_2, and thus we conclude that there is a new intermediate long range ordered phase in the narrow temperature region between the fcc and the fct phase. Because this phase also appeared reversibly upon heating and the intensity of each peak did not change while its temperature was kept in the intermediate region for about two days, it is believed to be the thermodynamically stable phase. The hysteresis within 1K was observed at the lower temperature phase transition which should be the weakly first order.

In order to clarify the structural characteristics of this phase, we investigated the splitting of Bragg reflections. As is depicted in Fig.

2-2-5, total of 44 peak positions seem to be consistently indexed by assuming two kinds of tetragonal lattices with different tetragonality. The lattice constants of these two lattices at 267.5K are;

a_1=3.795Å, c_1=3.648Å, (c_1/a_1=0.961),

a_2=3.766Å, c_2=3.737Å, (c_2/a_2=0.992),

Other possibilities, such as orthorhombic, monoclinic, or other low symmetry structure did not give any consistent agreement with the observed distribution of the Bragg positions. Moreover, since any peaks did not exist around the points $(110)_{fcc}$, $(330)_{fcc}$, etc., the symmetry of this phase should not be lower than tetragonal. We conclude that the intermediate phase between fcc and the low temperature fct phase is characterized by the mixture of two different types of tetragonal lattices. The evidence that each reciprocal lattice does not distribute throughout the reciprocal lattice plane indicates the macroscopically largeness of each grain with one primary axis.

In the first experiment summarized in Fig.2-2-3, the peak corresponding to the lattice constant c_1 was absent. This would be due to the fact that the irradiated area did not contain such a region because the beam was too narrow. In order to establish the "two-tetragonal-mixed phase", it is important to observe four peaks in the intermediate temperature region within the same experimental setting, and to reproduce the same results using different crystals. For this purpose we also investigated the temperature dependence of a $(200)_{fcc}$ peak for the sample nominally containing 30.2 at%-Pd using

the instrument with an Fe-target tube, a PG(002) monochromator and a slit system with 0.5mm wide and 2.0mm high. (As is depicted in Fig.2-1-1(b).) Since the beam divergence from PG(002) is considerably broader than that from Ge(111), the irradiated area was about 100 times larger than that of the previous high resolution experiment. With this wider resolution, all possible domains with different orientations are expected to be included in the irradiated area. As a result, a $(200)_{fcc}$ Bragg reflection split into four peaks in the intermediate temperature range and then transformed into the two peaks which corresponds to the pure low temperature tetragonal structure (see Fig. 2-2-6). The transition temperatures are determined as T_1=263K and T_2=253K, respectively.

This result supplements the shortage in the result of high-resolution experiment given in Fig. 2-2-3 and confirmed the existence of the "two-tetragonal-mixed" intermediate phase.

C. Results on the crystals with higher Pd concentrations

The same (high resolution) type of experiments were carried out for the samples nominally containing 30.8 at%-Pd and 31.2 at%-Pd. As was mentioned in §2-1, these samples tend to be heterogeneous in concentration distribution. This was shown by the result of the chemical analysis and also by neutron diffraction in which smearing of the transition temperature over 100K were observed. In X-ray diffraction, it was observed that there existed many grains with large angle mosaic distribution. When the slit

system was removed for the whole crystal to be irradiated, the profile of the diffraction of ω-scanning showed a "multi-peaks profile". Each of them had its own transition temperature indicating the sample was heterogeneous. However, curiously, we observed only one kind of peak in the low temperature phase, which means the grains reorientated below the transition temperature.

Using narrow slits (0.5mm wide and 1.0mm high) so as to radiate only one grain, we observed the temperature dependence of the position of (600) Bragg peak and its line profile in the direction of [100]. As is shown in Fig. 2-2-7, the feature of the peak splitting was not the same as the previous case of the sample containing 30.1 at%-Pd. (Fig 2-2-2). The magnitude of the splitting in an intermediate temperature regime (224K ~ 201K), was so small that the splitting into separated peaks could not be identified but only broadening of the peak occurred. The possibility that there were several domains having different transition temperatures was ruled out since the fundamental reflection of the low temperature phase gave single sharp peak. Therefore, the indication of the existence of the intermediate phase in this sample is only seen in the broadening of the peak. Fig. 2-2-8 shows the temperature variation of the lattice constant defined by the position of (600) Bragg reflection and the full-width-at-half-maximum (FWHM) of this reflection for the specimen whose nominal composition was 31.2 at%-Pd. From these results, we determined the two transition temperatures as T_1=224K and T_2=201K. Similar results were obtained from the experiment for

the specimen nominally containing 30.8 at%-Pd. The transition temperatures were determined to be T_1=226K and T_2=204K.

The results are summarized in Fig. 2-2-9. The intermediate temperature regions are indicated by the meshed lines between the two transition temperatures. The horizontal axis indicates the nominal composition of palladium. The transition points as determined from the two results with higher concentration side may not be exact because their real concentrations were not known as was mentioned in §2-1. The overall concentration dependence of the transition temperatures are consistent with the result by Sugiyama *et al.*[33] (indicated by the solid line), which was determined by the surface relief in optical micrographs.

§2-3. Neutron Scattering Measurements

A. Experimental details

We also carried out neutron scattering experiments. For this purpose, a circular cone single crystal about 0.5cc in volume and having nominal composition 30.2 at%-Pd was cut from an original ingot. It could be conveniently oriented to measure scattering in the (hk0) plane with the c^*-axis of the cubic lattice perpendicular to the scattering plane. The measurements were performed on the HT-8 triple-axis spectrometer at the Japan-Research-Reactor-2 of the JAERI TOKAI. Pyrolytic graphite (002) reflection was used as both double monochromators and the analyzer. Collimations were selected as 40'-(80'-40')-S-20'-A-40' for investigating the splitting of the Bragg peak and 40'-(80'-80')-S-40'-A-40' for observing the phonon spectra. A fixed incident energy of 13.7 meV with a PG filter was utilized for observing the splittings of the Bragg peaks. Incident energy of 30.7 meV with a PG filter was used for the observation of phonons. (See Fig.2-3-1.) The crystal was mounted in a closed-cycle helium refrigerator (CTI-Cryogenics) and the temperature of the sample was monitored by Si-diode sensor and controlled so that the temperature fluctuation was less than ±0.7K.

B. Temperature dependence of (200) reflection

The temperature dependence of the peak intensity of (200) Bragg was observed in order to confirm the existence of the intermediate phase throughout the bulk of the crystal, making use of

the advantage of neutron scattering which gives the bulk informations. Unfortunately the splitting of peaks in this phase is so small and the divergence of the neutron beam was so broad that the "multi-peaks profile" was not observed by neutron scattering measurements.

We expected that the profile must become broad and the peak height must decrease in the intermediate phase, since the Bragg reflections of the cubic phase should split into several peaks at T_1. When the temperature reaches to T_2, the lattice transforms to the low temperature tetragonal phase and constructs the twin structure. Therefore, the fundamental Bragg reflections of the tetragonal lattice move off from the scattering plane and the peak heights in the scattering plane decrease further. The observed temperature variation of the (200) Bragg reflection is shown in Fig.2-3-2. The increase of the intensity above 263K as decreasing temperature is thought to be due to the increase of quasi-elastic scattering intensity (discussed later). The decrease of the peak intensity below 263K seem to indicate small splittings of the $(200)_{fcc}$ peak into $(200)_1$, $(200)_2$, $(002)_1$, $(002)_2$* at T_1. At 253K, the peak intensity decreased more steeply.

From these results, we could determine the two transition temperatures; T_1=263K and T_2=253K. This is consistent with the result of the X-ray diffraction (see Fig. 2-2-6). Therefore, we conclude that

---

* Subscripts denote two different tetragonal lattices.

the intermediate phase exists throughout the whole crystal. That is, the two-tetragonal mixed state is not just a surface effect, but an intrinsic thermal equilibrium phase.

C. Temperature dependence of the [110]TA phonon

The dispersion relation of [110]TA phonon branch and its temperature variation were observed. The previous investigation by Sato et al.[35] showed a slight softening of the [110]TA_1 branch around the Γ-point or a decrease of the elastic constant $(c_{11}-c_{12})/2$ as the temperature is lowered. However, they could not study the detailed behavior of the soft phonon near the transition temperature because of smearing of the transition temperature over a range of 35K. The sample prepared for the present study was sufficiently homogeneous to investigate the lattice dynamics near the phase transition point. The experiment were performed with a constant initial energy of 30.7 meV, and collimations of 40'-(80'-80')-S-40'-A-40' were used. (See Fig.2-3-1(b).) Observations of inelastic scattering spectra were carried out around the $(220)_{fcc}$ reflection.

The dispersion curve of [110]TA phonon branch at room temperature and just above T_1 is shown in Fig.2-3-3. The result is consistent with that of Sato *et al.*[35] In the observed q-region ($|q|\geq 0.15$), phonon softening was not remarkable. We could not access closer to the Γ-point where the softening is expected to occur clearly because of the limitation of the instrumental resolution. In order to observe the low-q region, it is necessary to use a high flux neutron

source.

One of the typical data of the observed spectra obtained by a constant q-scan at q=0.2 and its temperature variation is presented in Fig. 2-3-4. The main-peak at E = 0 meV (the shift is not intrinsic) is quasi-elastic scatterings, and the sub-peak at about E = 4 meV is caused by a phonon. The open circles and the dotted line represent the profile at 292K, far above T_1, the full triangles and the solid line just above T_1, and the open squares and dashed line just above T_2, in the intermediate phase. The characteristic feature around the transition point is seen in the properties of quasi-elastic scattering. Its temperature dependence is summarized in Fig.2-3-5. Although the intensity at q=0.1 is influenced by the [110] soft phonon, the quasi-elastic scattering at q=0.2 is separated with the soft phonon. Both the increase of the quasi-elastic scattering and the softening of phonon occur simultaneously up to T_1, and they slightly decrease between T_1 and T_2 and vanish below T_2. It means that both the static and dynamic deformation increase simultaneously above the phase transition point T_1.

§2-4. Huang Scattering

It was pointed out by Yamada[38] that even at first order phase transitions, where there is no critical fluctuations, diffuse 'quasi-elastic' scattering may be observed. This is interpreted as Huang scattering due to random distribution of 'embryos' of the low temperature structure which is 'dressed' by strain fields. The increase of Huang scattering above the transition point can be understood as the increase of the number of the embryos. This effect was observed by X-ray and/or neutron scattering measurements in various materials such as $K_2PbCu(NO_2)_6$[39], Fe_3O_4,[40-42] etc. From the theory of Huang scattering, the shape of the diffuse scattering around a Bragg point gives the information of the symmetry of the point defect or the cluster which deforms surrounding lattice.

We also observed the X-ray Huang scattering in Fe-Pd and its temperature variation in and above the intermediate phase for the sample nominally containing 30.1 at%-Pd. The instruments with Fe-target X-ray source, PG(002) monochromator and PSPC were effectively utilized for this experiment. (See Fig.2-1-1(b).) The intensity contours around (200) and (220) in (hk0) plane at room temperature are depicted in Fig. 2-4-1. The obtained diffuse scattering is running along [110] and $[1\bar{1}0]$ direction around (200) Bragg reflection, and along $[1\bar{1}0]$ direction around (220) Bragg reflection. The results consistent with the Huang scattering due to a "point defect" with tetragonal symmetry. The close relationship of the

observed Huang scattering and the phase transition can be shown by observing the temperature dependence of the profile and the intensity. The diffuse pattern around (200) in (hk0) plane at various temperatures are depicted in Fig. 2-4-2. Although the monotonically changing background contaminates, the component running along [110] and $[1\bar{1}0]$ direction increases toward T_1 (=273K) and then decreases. This suggests that the Huang scattering is not due to the ordinary defects such as impurity, vacancy etc. but mainly due to local lattice deformation as precursor to the phase transition. In order to distinguish the component which is relevant to the phase transition from the irrelevant component, subtraction of the data at room temperature (Fig.2-4-2(a)) from the data at 275K (Fig.2-4-2(b)) was carried out, and the result is shown in Fig.2-4-3. The sharp streaks running in the directions of [110] and $[1\bar{1}0]$ are identified as the component related to the phase transition. Taking into account the results of neutron scattering given in the previous section, it is concluded that this component primarily corresponds to the central peak (quasi-elastic), although in the low-q region the contamination of the soft phonons must not be neglected.

It is necessary to pay attention to the existence of the component which monotonically depends on the temperature. The preliminary experimental result for the sample nominally containing 30.2 at%-Pd by the quasi-elastic neutron scattering at the room temperature and 373K are depicted in Fig. 2-4-4. There are also Huang type scatterings around (200) Bragg reflection in the (hk0)

plane similar to Fig. 2-4-3. Rather intense diffuse scattering remained even at 373K, which is about 110K higher than the first transition temperature. It increases as the temperature increases. Comparing with the result of Sugiyama *et al.*[33], that the "tweed pattern" starts from about T_m+100K, we can conclude that the component extending broadly and the powder line places at $q \cong 1.8$ have no relation with the precursor phenomena and/or the phase transition.

Therefore, the Huang scattering and their temperature variation have to be considered by excluding the component monotonically changes with the temperature.

§3. Possible Origins of the Intermediate Phase: Crest-riding Periodons

The most remarkable point of the present experimental results is that a new intermediate phase appears between the uniform fcc and fct phases. This intermediate phase is characterized by a mixture of two tetragonal lattices with different tetragonalities. It is likely that the two kinds of lattices coexist coherently, rather than existing as a simple incoherent mixture of the two different phases.

The incommensurate phase (IC-phase) which has been studied extensively in various fields of physics seems to give a useful reference to understand the origin of stability of the new intermediate phase. The IC-phase often exists in a narrow temperature range between the two kinds of commensurate ordered structures. It is a kind of spatially modulated structure, which may be characterized by regular array of solitons (domain boundaries) separating commensurate structures. In order to understand IC phases, it is essential to introduce an **r**-dependent (**r** means a position vector) order parameter. The stability of the system is then examined using Ginzburg-Landau type free energy expansion. This has become the standard technique to discuss the formation of the IC-phase of various kinds.[43)]

In connection with first order phase transitions, several authors recently pointed out that when the order parameter is allowed to be spatially varying, a modulated state may be stabilized as an

intermediate phase before the uniform ordered phase is stabilized.[44]

Falk[45] first dealt with martensite transformations on a simple one-dimensional model restricted to one habit plane and to a shear strain ($e(x)$) in that plane. As is outlined in Appendix A, he has obtained very interesting solutions of $e(x)$ in the vicinity of the first order transition point. These solutions give a kind of modulated structure which is essentially expressed by a mixture of two different kind of e-values. As is depicted in Fig.A-4, the amplitudes of strain e_1 and e_2, are smaller than the value e_0 which is realized in the low temperature phase. These are certainly reminiscent of our experimental results.

Barsch and Krumhansl[46] extended Falk's treatment to the case of 2D system (deformation is restricted within 2-dimensions) which transforms from tetragonal (4mm) to orthorhombic (2mm). They also found the solution expressed by a coherently modulated structure with different orthorhombicities, which they call a "crest-riding-periodon" state. Therefore, our intermediate phase seems to be interpreted as the "crest-riding-periodon" structure.

We try to apply the idea explained above to the present system. There is an important difference, however, between the previous models and our system. In both 1D and 2D systems discussed by Falk[45] and Barsch and Krumhansl[46], respectively, the order parameter is assumed to be a single independent strain component. On the other hand, in our case of fcc-fct transition, one can not specify a single independent strain component as the order parameter: It is well-

known that the fcc-fct transition, which is induced by the lattice instability against the [110] shear, is explained by taking the two strain components u_2 and u_3 as the order parameters;

$$u_2=(2^{-1/2})(e_{xx}-e_{yy}),$$
$$u_3=(6^{-1/2})(2e_{zz}-e_{xx}-e_{yy}). \tag{3-1}$$

These two strain components form the basis functions of the two-dimensional irreducible representation E_g of the cubic point group m3m. Taking notice of this essential difference, we follow the similar procedure developed by Falk[45] and Barsch and Krumhansl.[46]

To begin with, let us review the conventional treatment of fcc-fct transition. The transition is discussed using the Landau free energy F given by[47-49]

$$F=\frac{a}{2}(u_2^2+u_3^2)+\frac{b}{3}(u_3^3-3u_2^2u_3)+\frac{c}{4}(u_2^2+u_3^2)^2 , \tag{3-2}$$

and by examining the thermodynamical stability of the system. This procedure simply gives ordinary first order phase transition where the low temperature phase is given by either one of the following equivalent states represented by

$$(u_3,u_2)=(-u_0\,,0)\,,(\frac{1}{2}u_0\,,\frac{\sqrt{3}}{2}u_0)\,,(\frac{1}{2}u_0\,,-\frac{\sqrt{3}}{2}u_0) , \tag{3-3}$$

with

$$u_0=\frac{b+\sqrt{b^2-4ac}}{2c} . \tag{3-4}$$

In the present treatment we allow the order parameters to be spatially varying, $u_2(\mathbf{r})$ and $u_3(\mathbf{r})$, and the stability of the system is discussed using the Ginzburg-Landau free energy functional $F[u_2(\mathbf{r}),u_3(\mathbf{r})]$;

$$F[u_2(\mathbf{r}),u_3(\mathbf{r})]=\int [\frac{\kappa}{2}\{(\frac{\partial u_2}{\partial \mathbf{r}})^2+(\frac{\partial u_3}{\partial \mathbf{r}})^2\}+U[u_2(\mathbf{r}),u_3(\mathbf{r})]]d\mathbf{r} \quad , \tag{3-5}$$

$$U[u_2(\mathbf{r}),u_3(\mathbf{r})]=\frac{a}{2}(u_2^2+u_3^2)+\frac{b}{3}(u_3^3-3u_2^2u_3)+\frac{c}{4}(u_2^2+u_3^2)^2 \quad . \tag{3-6}$$

In order to find proper solutions, we impose the constraint:

$$\int u_\nu(\mathbf{r})d\mathbf{r}=0, \qquad \nu=2,3 \quad , \tag{3-7}$$

which means that the total volume of the system is kept invariant. When the local strains are small enough, this should be a reasonable assumption since each mosaic crystal is mechanically constrained by the surrounding grains.

Barsch and Krumhansl[50] discussed similar problem in connection with the twin boundary formation in the tetragonal phase of ferroelastic materials. They have given a particular solution explicitly as

$$u_2=\frac{\sqrt{3}}{2}u_0\tanh[(s-s_0)/\sqrt{2}] \quad , \tag{3-8}$$

$$u_3=\frac{1}{2}u_0 \quad ,$$

$$(s=\bar{\mathbf{n}}\cdot\mathbf{r} \ , \ \bar{\mathbf{n}}//[110]) \ ,$$

at the reduced temperature $\tau = (T-T_0)/(T_c-T_0) = -9$, where T_0 is the stability limit of the cubic phase.

In order to understand the properties of the solution, it is convenient to draw the trajectory of the 'motion' of the representative point $(u_3(\mathbf{r}), u_2(\mathbf{r}))$ in the two-dimensional (u_3, u_2) space as the spatial coordinate $\mathbf{r}$ is varied. The trajectory corresponding to the above solution is given by the straight lines connecting a pair of the three equilibrium states given by eq.(3-3). (See Fig.3-1(a).) This is certainly valid when the temperature is lower than T_0 (Regime IV).

In the temperature region $T \sim T_c$ (regime (II) and (III)), in which we are interested, the potential $U[u_2, u_3]$ has another minimum at the origin (0,0) of the (u_3, u_2) space, corresponding to the undistorted cubic state. (See Fig.3-1(b).) We can see intuitively that when $T \sim T_c$, the trajectory would be modified so that it will pass by this center minimum.

Keeping this in mind, we seek for the appropriate solutions at $T \sim T_c$. For simplicity, we consider that u_v's depend only on one component, x, of the spatial coordinates. The Euler equations to be solved are:

$$\kappa \frac{\partial^2 u_2}{\partial x^2} - a u_2 + 2b u_3^2 - c u_2 (u_2^2 + u_3^2) = 0 \quad , \qquad (3\text{-}9)$$

$$\kappa \frac{\partial^2 u_3}{\partial x^2} - a u_3 + b(u_2^2 - u_3^2) - c u_3 (u_2^2 + u_3^2) = 0 \quad .$$

Instead of trying to find the analytic solutions of these equations, we

calculate numerically $u_2(x)$ and $u_3(x)$, and whence the trajectory, following the method developed by Ishibashi et al.[51-53] We adopt the following boundary conditions:*

$$(u_3,u_2)=(\frac{1}{2}u_0\,,\,\frac{\sqrt{3}}{2}u_0) \qquad \text{at } x = N\Delta x\,,$$
$$(u_3,u_2)=(\frac{1}{2}u_0\,,\,-\frac{\sqrt{3}}{2}u_0) \qquad \text{at } x = -N\Delta x\,, \tag{3-10}$$

where Δx is the increment of x and $\pm N\Delta x$ stands for $x\rightarrow\pm\infty$, or the edges of the system. The choice of this boundary condition seems to be valid as long as the tetragonal state has the minimum energy. This point will be discussed later in more detail.

Several of the typical examples of the results are shown in Fig.3-2. Just as expected, the trajectory has been modified so that it passes through the points close to the origin. Notice the trajectory does not pass through exactly the minimum point (0,0) (cubic state). This is due to the following intrinsic asymmetry of the system we are considering: Since the order parameters belong to the two-dimensional representation of the cubic point group m3m, the potential has threefold symmetry in two-dimensional (u_3,u_2) space. This causes the asymmetry of the potential along the u_3 axis, whence the trajectory should go through slightly off (0,0) as it traverses the u_3-axis.

---

* Physical meaning of this boundary condition is to freeze the two variants of low temperature structure at $x\rightarrow\pm\infty$. Either pairs of the three variants given in eq.(3-3) can be taken as possible boundary state.

At this stage, the readers may notice that $u_3(x)$ as given in Fig.3-2 does not satisfy the constraint given by eq.(3-7). However, as is mentioned in the footnote, starting from the other two equivalent sets of boundary conditions, and superimposing the results with equal weight, we obtain a trajectory satisfying the threefold symmetry in the (u_3,u_2) space. Correspondingly, the constraint becomes automatically satisfied.

In Fig.3-2, it should be noted that we have plotted the representative points with equal interval of x, whence the density of the points on the trajectory directly indicates the length of persistence of the state in the space. Since the positions of high density are located at $(u_0',0)$ as well as at $(u_0/2, \pm 3^{1/2}u_0/2)$ in Fig.3-2, we can clearly see that the stable state in the temperature region of $T \sim T_c$ is practically given by a coherent mixture of the two tetragonal lattices with c/a-ratios;

$$c_1/a_1 = 1 - \frac{\sqrt{3}}{\sqrt{2}}|u_0| \quad , \qquad (3\text{-}11)$$

$$c_2/a_2 = 1 + 3\sqrt{6}|u_0'| \quad ,$$

where $|u_0'|$ is one order of magnitude smaller than $|u_0|$ (see Fig.3-2). This seems to explain the essential origin of the stabilization of the two tetragonal lattices observed in the pretransitional state of $Fe_{1-x}Pd_x$.

However, there is an important discrepancy between the observed tetragonalities and those given in eq.(3-11). The observed

value of c_2/a_2 (which is closer to unity) is 0.992. On the other hand, the value given in eq.(3-11) is larger than unity.

One of the possibilities to reconcile this discrepancy is to introduce the higher order terms in the expansion of the free energy functional with respect to u_2 and u_3. We add th 5th-order and the 6th-order terms to the local potential U;*

$$U'[u_2(\mathbf{r}),u_3(\mathbf{r})]=\frac{d}{5}(u_3^3-3u_2^2u_3)(u_2^2+u_3^2)$$
$$+\frac{e_1}{6}(u_2^2+u_3^2)^3+\frac{e_2}{6}(u_3^3-3u_2^2u_3)^2 , \qquad (3\text{-}12)$$

which satisfies the symmetry requirement of the point group m3m. Taking the 5th-order term into account, the center minimum of the potential tends to shift to negative u_3 (and equivalent) directions by an amount u_0'' ($u_0''\ll u_0$). The additional parameters are chosen so that the boundary states remain to be the same as the previous computations.

Some of the typical examples of the calculated $u_2(x)$ and $u_3(x)$, the trajectories, and the resultant c/a-ratios are given in Fig.3-3. As is clearly seen in the figure, we now have two locally stable tetragonal states (expressed by the high density positions of the representative points on the trajectory) with the tetragonalities;

$$c_1/a_1 = 1-\frac{\sqrt{3}}{\sqrt{2}}|u_0| , \qquad (3\text{-}13)$$

*The term of essential importance is the 5th-order term. The 6th-order term is necessary in order to certify the stability of the system against the infinitely large u_v-value.

$$c_2/a_2 = 1 - \frac{\sqrt{3}}{\sqrt{2}}|u_0''| ,$$

in the temperature region close to T_c. As the temperature is lowered, the second tetragonal lattice given by (a_2,c_2) disappears. (See Fig.3-3(b).)

The overall feature of the temperature dependence of the lattice constants is given schematically in Fig.3-4, which is consistent with the experimental results.

§4. Possible Origin of Huang Scattering: Embryonic Fluctuations

In the preceding section, we have obtained 'periodon' solution using the boundary condition given in (3-10), that is,

$$(u_3,u_2)=(\frac{1}{2}u_0\,,\,\frac{\sqrt{3}}{2}u_0) \qquad \text{at } x=N\Delta x\,,$$

$$(u_3,u_2)=(\frac{1}{2}u_0\,,\,-\frac{\sqrt{3}}{2}u_0) \qquad \text{at } x=-N\Delta x\,,$$

In the temperature regime (III) this is certainly valid, since the states $(u_0/2,\ \pm 3^{1/2}u_0/2)$ represents the absolute minima (the lowest energy states). In regime (II), however, it may not physically plausible to impose the same boundary condition because in this temperature regime the above states are the secondary minima (metastable states) rather than the lowest energy state.

We consider that the appropriate boundary condition to be adopted in this regime would be

$$(u_3,u_2)=(0\,,0) \qquad \text{at } x=\pm N\Delta x\,, \tag{4-1}$$

$$(u_3,u_2)=(\frac{1}{2}u_0\,,\,\frac{\sqrt{3}}{2}u_0) \qquad \text{at } x=x_0\,,$$

where x_0 is an arbitrary position. We performed the similar numerical calculations using the above boundary conditions. In this case, the trajectory simply gives a 'star' centered at (0,0) as is shown in Fig.4-1. In the physical space, this just corresponds to the state where an isolated small tetragonal region or the 'embryo' of the low

temperature phase is sitting at $x=x_0$ within the parent cubic matrix (see the right part of Fig.4-1). Therefore in the regime (II), the total system is viewed as random distribution of embryonic fluctuations in the parent phase.

In this connection, it is noticeable that we observed strong Huang scattering in the temperature region just above the "two-tetragonal-mixed" phase. This definitely suggests that the observed strong Huang scattering is due to the embryos of the low temperature phase which behaves like "tetragonal defects" in a elastic medium.

We tried to analyze the intensity distribution of the Huang scattering, in particular of the temperature dependent component. For the analysis, it is convenient to use the theory developed by Dederichs.[54] (See Appendix B.) As is given in Appendix B, the intensity of Huang scattering is given by

$$S_{\mathrm{Huang}}(\boldsymbol{K}) = cN\,|f|^2(h/qV_c)^2(\gamma^{(1)}(\kappa)\Pi^{(1)} + \gamma^{(2)}(\kappa)\Pi^{(2)} + \gamma^{(3)}(\kappa)\Pi^{(3)}),$$

with

$$\gamma^{(1)}(\kappa) = (T_{11}+T_{22}+T_{33})^2/3,$$

$$\gamma^{(2)}(\kappa) = \{(T_{11}-T_{22})^2+(T_{22}-T_{33})^2+(T_{33}-T_{11})^2\}/3,$$

$$\gamma^{(3)}(\kappa) = \{(T_{11}+T_{22})^2+(T_{22}+T_{33})^2+(T_{33}+T_{11})^2\}/2,$$

$$T_{ij}= \Sigma_l \eta_l \zeta_{li}(\kappa)\kappa_j,.$$

The numerical values of c_{ij}'s experimentally obtained by Sato *et al.*[35]

$$c_{11} = 1.4 \times 10^{12}\ \mathrm{dyn/cm^2}$$

$$c_{12} = 1.34 \times 10^{12} \qquad (4\text{-}2)$$

$$c_{44} = 0.8 \times 10^{12}$$

are used for the calculations of Huang scattering. When a tetragonal

defect which is represented by the double force tensor P;

$$P = \begin{pmatrix} -1 & & O \\ & -1 & \\ O & & 2 \end{pmatrix}, \tag{4-3}$$

is assumed, the calculated intensity contours of Huang scattering is given in Fig.4-2. Similarly, the calculations for the case of isotropic defect which is represented by

$$P = \begin{pmatrix} 1 & & O \\ & 1 & \\ O & & 1 \end{pmatrix}, \tag{4-4}$$

are carried out. The results are given in Fig.4-3.

Comparing with the experimental data, we can conclude that the temperature dependent part of Huang scattering is due to the 'tetragonal' defect, while the temperature independent component is due to an isotropic defect. Therefore, the intensity increase of the sharp streaks running to the [110] and $[1\bar{1}0]$ direction above the first transition temperature (T_1) is considered to indicate the increase in the number of the tetragonal 'embryos' in the cubic matrix. This phenomena occur in accordance with growing of the "tweed pattern" observed by transmission electron microscopy. Therefore, we may infer that the "tweed pattern" is caused by the strain contrast which is accompanying the tetragonal embryos, as is suggested by Ohshima *et al.*[34)]

§5. Conclusion and Discussions

A. Conclusion

We performed the precise X-ray and neutron scattering measurements on Fe-Pd alloys containing about 30.1, 30.2, 30.8, and 31.2 at%-Pd in order to investigate their fcc-fct martensitic transformation. The results of the experiments are summarized as follows:

(i) In the intermediate temperature range ($T_2<T<T_1$) between fcc and fct phase, we observed complicated splitting of Bragg reflections which indicated that there is an intermediate phase before the crystal transforms to fct structure.

(ii) Just above the upper transition temperature (T_1), diffuse X-ray scattering and quasi-elastic neutron scattering were observed. The intensity was highly anisotropic extending along [110] directions. The intensity increased towards T_1 as the temperature was decreased.

By analyzing the experimental results, we concluded that:

(i) The intermediate phase is characterized by coexistence of two tetragonal lattices with different tetragonalities.

(ii) The origin of the stability of this two-tetragonal-mixed phase has been investigated theoretically by extending Barsch and Krumhansl's treatment.[50] It has been shown that the observed intermediate phase could be interpreted as an extended version of "crest-riding periodon" structure proposed by Falk[45] and Barsch and Krumhansl.[46]

(iii) The characteristics of anisotropic distribution of Huang scattering indicate that the origin of Huang scattering is the local lattice distortion having tetragonal symmetry, which implies there are many embryos of the low temperature structure distributed randomly in the temperature region of $T>T_1$.

From these considerations, we infer the process of first order martensite transformation in Fe-Pd alloys as follows: cubic phase (regime (I)) → random distribution of tetragonal embryos (regime (II)) → two-tetragonal-mixed phase (regime (III)) → tetragonal phase with variants separated by sharp domain boundaries (regime (IV)).

B. Discussions

Our numerical solution obtained in §3 seems to be a natural extension of the previous treatments on single order parameter models to the case of fcc-fct transition where the relevant strain components construct the E_g representation (doubly-degenerate order parameters), and the obtained solution is a two order parameter version of the "crest-riding periodon". However, there seem to exist two crucial difficulties in our treatment.

(i) Very recently, Barsch[55] pointed out that the solution which is represented by the trajectories given in Fig.3-3 may contradict to the "elastic compatibility" conditions which should be satisfied by any elastic continuum. The violation of the elastic compatibility means that, as the system follows the trajectory, some sort of topological defects should be inevitably introduced within the medium which

will cost finite defect formation energy. In order to avoid this difficulty, we have to take into account other strain components such as;

$$u_1=3^{-1/2}(e_{xx}+e_{yy}+e_{zz}),$$
$$u_4=e_{yz}, \qquad (5\text{-}1)$$
$$u_5=e_{zx},$$
$$u_6=e_{xy},$$

into the free energy expression eq.(3-2), since the compatibility requires strong couplings between u_2 and u_3, the order parameter, and those strains u_1, u_4, u_5 and u_6 which are not associated with the phase transition. These couplings may change the lowest energy path drastically. This point is left for the future problem to be examined.

(ii) In our treatment, introduction of the higher order (5th and 6th) terms are necessary to obtain two tetragonal lattices both having c/a<1 in accordance with the experiments. (Without these terms, solutions gives one of the tetragonal lattice with c/a>1.) The "crest-riding periodons" are discussed without including such higher-order effect. It would be more satisfactory if the experimental results are explained within the framework of the original treatment, which does not include higher order terms.

It is noticed that the "crest-riding-periodon" picture as presented by Falk[45)] would be subjected to reconsideration in the temperature range $T>T_c$. Falk obtained the periodon solution with the boundary conditions $\partial e/\partial x=0$ (couple stress=0). At the same time, the energy density is taken to be $f=f_0$ with f_0 a finite positive value

when $T>T_c$. When integrated over the space, this would imply that the energy of the periodon state is appreciably high as compared with the thermal equilibrium state (f=0 throughout the space). This difficulty is manifested in his solution in an unbounded system. As is shown in Fig.5-1, the strain $e(x)$ as obtained by Falk has the properties;

$$e(x)=e_0 \text{ as } x\rightarrow\pm\infty,$$
$$e(x)\sim 0 \text{ at } x=0. \tag{5-2}$$

That is, major part of the system including boundaries takes the structure of the low temperature phase while only a small region around $x\sim 0$ takes on the structure close to the high temperature phase, which means that micro-region of the high temperature phase is included in the matrix of the low temperature phase.

On the other hand, the 'embryo' solution given in the preceding section is physically more plausible: As depicted in Fig.4-1, it merges into the high temperature (cubic) structure as $x\rightarrow\pm\infty$, and takes on the tetragonal structure only in the vicinity of $x\sim 0$. This is certainly consistent with our physical intuition that there will be micro-region of the low temperature phase distributed randomly in the mother matrix at $T\geq T_c$. Not only that the experimental results on Huang scattering in the region of $T>T_c$, agree with the above picture as is discussed in §4. Therefore, as far as the temperature region II ($T_c<T<T_0'$) is concerned, the treatment developed in §4 gives satisfactory basis for the present experimental results on Huang scattering.

Appendix A

Falk[45] dealt with martensite transformations on a simple one-dimensional model restricted to one habit plane and to a shear strain in that plane in one direction only.

In a reduced scale, the Landau free energy density functional describing the first order transition is expressed by

$$F_L(e,T)=e^6-e^4+(T+1/4)e^2 \qquad \text{(A-1)}$$

where e and T denote the reduced shear strain and the reduced temperature, respectively. The temperature variation of this free energy is easily seen by plotting F_L as a function of shear strain e at various temperatures T. At high temperature (T>1/12) the Landau free energy has one minimum at e=0 corresponding to the fact that only austenite is stable. At low temperature (T<-1/4) there is no austenite minimum at e=0, and are two minima at $e=\pm e_0(T)$ corresponding to martensite phases. At intermediate temperature (-1/4<T<1/12) the free energy has three minima, that is, both martensite variants as well as austenite are stable or at least metastable. At T=0 all the minima are of equal depth. As usual, he includes the strain gradient term to constructs a Ginzburg-Landau free energy density,

$$F(e,e',T)=F_L(e,T)+e'^2 \qquad \text{(A-2)}$$

where the prime denotes the derivative with respect to the reduced coordinate x.

If there is no external force the equilibrium configuration $e(x)$ is

determined by the minimum of the total free energy. The corresponding Euler-Lagrange equations are;

$$\frac{\partial F}{\partial e} - \frac{d}{dx}\frac{\partial F}{\partial e'} = 0 \quad . \quad x \in [x_1, x_2] \tag{A-3}$$

He selected boundary conditions that the couple stress

$$\mu = \frac{\partial F}{\partial e'} = 2e' \quad , \tag{A-4}$$

due to lattice curvature is zero, i.e. the lattice curvature vanishes at the boundary:

$$\mu(x_1) = \mu(x_2) = 0. \tag{A-5}$$

Equation (A-3) yields with eq.(A-4)

$$\frac{\partial F}{\partial e} = \mu' = 2e'' = 2\frac{de'}{de}e' \quad , \tag{A-6}$$

and, by further integration

$$e' = \sqrt{F_L(e) - F_0} \quad . \tag{A-7}$$

Taking the boundary condition eq.(A-5) into consideration, the free energy density takes the same value F_0 at both of the boundaries.

$$F_L(x_1)=F_L(x_2)=F_0. \tag{A-8}$$

In addition we must have

$$F_L(x)>F_0, \ x \in (x_1,x_2). \tag{A-9}$$

Equation (A-7) can be integrated to give the inverse function of $e(x)$ namely

$$x(e) = \int \frac{de}{\sqrt{F_L(e) - F_0}} = \int \frac{de}{\sqrt{e^6 - e^4 + (T + 1/4)e^2 - F_0}} \quad . \tag{A-10}$$

The function $x(e)$ can be expressed by elliptic integrals the evaluation of which depends on the reduced temperature T and on the parameter F_0.

In the case of T<0 and F_0<0, he showed the conventional solution which includes two kinds of martensite regions (positive and negative side of the potential curve) and domain walls separating them. (See Figs. A-1 and A-2.)

More interesting case he showed is for -1/4<T<1/12 and F_0>0. The radicand of (A-10)

$$F(e)-F_0=e^6-e^4+(T+1/4)e^2-F_0=0 \tag{A-11}$$

has three pairs of real roots $\pm e_1$, $\pm e_2$, $\pm e_3$. Let these values as $0<e_1<e_2<e_3$. Because there are restrictions expressed by eqs (A-8) and (A-9), strain $e(x)$ can vary within the bold part of the curve depicted in Fig.A-3. And his solutions are shown in Fig.A-4 schematically. It means there is a kind of spatially modulated phase in the intermediate temperature region during homogeneous austenite and martensite. And the system fluctuate between the two state, the one is higher order of martensite, and the other is lower order one.

Appendix B

The results of Dederichs[54] are summarized as follows:

The scattered intensity for a momentum transfer $\boldsymbol{K}$ is given by

$$S(\boldsymbol{K}) = < \Sigma_{m,n} f_K^m f_K^n \exp\{i\boldsymbol{K}\cdot(\boldsymbol{R}^m-\boldsymbol{R}^n)\}> \tag{B-1}$$

for the elastic scattering, where $f_K{}^m$ is the atomic form factor and $\boldsymbol{R}^m$ is the position vector, both of them are of an atom m. By subtracting the Bragg intensities, the diffuse intensities are obtained by:

$$S_{diff}(\boldsymbol{K}) = \Sigma_{m,n} [<f_K^m f_K^n \exp\{i\boldsymbol{K}\cdot(\boldsymbol{R}^m-\boldsymbol{R}^n)\}> - <f_K^m \exp(i\boldsymbol{K}\cdot\boldsymbol{R}^m)> <f_K^n \exp(i\boldsymbol{K}\cdot\boldsymbol{R}^n)>] \ , \tag{B-2}$$

For small defect concentrations it become:

$$S_{diff}=cN\ |F(\boldsymbol{K})|^2 , \tag{B-3}$$

with

$$F(\boldsymbol{K})=f_K{}^D + f_K \Sigma_{m,n} \exp(i\boldsymbol{K}\cdot\boldsymbol{S}^n)\{\exp(i\boldsymbol{K}\cdot\boldsymbol{t}^n)-1\} , \tag{B-4}$$

where $f_K{}^D$ is the atomic scattering factor of point defects, $\boldsymbol{S}^n$ is the average atomic position, and cN is related to the number of defects. The displacement field $\boldsymbol{t}^n$ is determined by a lattice statics:

$$t_i{}^n = \Sigma_{m,j} G_{ij}{}^{n-m} P_j{}^m , \tag{B-5}$$

Here $G_{ij}{}^{n-m}$ is the harmonic Green function and $P_j{}^m$ is the force exerted due to the defect on the atom m. For large distance $\boldsymbol{R}^n$ from the defect, lattice statics goes over into continuum theory. Then it becomes,

$$t_i(\boldsymbol{R}\ )=-\Sigma_{l,j}\partial X_l G_{ij}(\boldsymbol{R}\ )P_{jl} \ , \tag{B-6}$$

with

$$P_{jl}=P_{lj} =\Sigma_m P_j{}^m X_l{}^m . \tag{B-7}$$

P_{jl} is the dipole tensor of defect, which indicates the symmetry of the defect.

If $\boldsymbol{h}$ is a reciprocal lattice vector of Bragg point and $\boldsymbol{q}$ is the deviation from the Bragg point, i.e. $\boldsymbol{K}=\boldsymbol{h}+\boldsymbol{q}$, $\exp(i\boldsymbol{K}\cdot\boldsymbol{R}^{n})$ in eq.(B-4) can be replaced by $\exp(i\boldsymbol{q}\cdot\boldsymbol{R}^{n})$. Further approximation, $\exp(i\boldsymbol{K}\cdot\boldsymbol{t}^{n})$ is also replaced by $\exp(i\boldsymbol{h}\cdot\boldsymbol{t}^{n})$. Then $\exp(i\boldsymbol{h}\cdot\boldsymbol{t}^{n})$ is separated to real and imaginary part, and obtained by neglecting terms proportional to $\boldsymbol{q}$;

$$F(\boldsymbol{K}) \cong f_K^{D} + f_K\Sigma_n\exp(i\boldsymbol{q}\cdot\boldsymbol{S})(\cos\boldsymbol{h}\cdot\boldsymbol{t}^{n} + i\sin\boldsymbol{h}\cdot\boldsymbol{t}^{n} -1)$$

$$\cong f_K^{D}-f_h\Sigma_n(1-\cos(\boldsymbol{h}\cdot\boldsymbol{t}^{n})) + if_h\boldsymbol{h}\cdot\tau(\boldsymbol{q}) \ , \qquad \text{(B-8)}$$

where $\tau(\boldsymbol{q})$ is the Fourier transform of $\boldsymbol{t}(\boldsymbol{R})$,

$$\tau_i(\boldsymbol{q}) = \Sigma_n\exp(i\boldsymbol{q}\cdot\boldsymbol{R}^{n})t_i(\boldsymbol{R}^{n}) \cong (1/V_c)\int d\boldsymbol{R}\ \exp(i\boldsymbol{q}\cdot\boldsymbol{R})\ t_i(\boldsymbol{R}). \qquad \text{(B-9)}$$

In considering eq.(B-6), $G_{ij}\infty(1/R)$ and $t_i(\boldsymbol{R}) \sim (1/R^2)$, then $\tau_i(\boldsymbol{q})$ becomes

$$\tau_i(\boldsymbol{q}) = (i/qV)\Sigma_{j,l}\ \zeta_{ij}(\kappa)\kappa_l P_{jl} \ , \qquad \text{(B-10)}$$

where $\kappa = \boldsymbol{q}/q$, $\kappa^2=1$ and $\zeta_{ij}(\kappa)$ is the inverse tensor of $\Sigma C_{ikjl}\kappa_k\kappa_l$.

In the cubic crystal, $c_{iiii}=c_{11}$, $c_{iijj}=c_{12}$, $c_{ijij}=c_{44}$ $(i,j=1,2,3)$ and $g_{ij}(\kappa)$ is given by[56)]

$$\zeta_{ij}(\kappa) = \frac{\delta_{ij}}{c_{44}+d\kappa_j^2} - \frac{\kappa_i\kappa_j}{(c_{44}+d\kappa_i^2)(c_{44}+d\kappa_j^2)} \times \frac{c_{44}+c_{12}}{\{1+\sum_l^3(c_{44}+c_{12})/(c_{44}+d\kappa_l^2)\kappa_l^2\}}$$

$$d = c_{11} - c_{12} - 2c_{44} \qquad \text{(B-11)}$$

Near to the Bragg reflection, the contribution from the term varies as $1/q^2$ is mainly, the diffuse intensity becomes

$$S_{\text{Huang}}(\boldsymbol{K}) = cN\ |f_h|^2\ |\boldsymbol{h}\cdot\tau(\boldsymbol{q})|^2$$

$$= cN\ |f_h|^2\ (h/q\ )|(1/V_c)\Sigma\eta_i\ \zeta_{ij}\ (\kappa\ )\kappa_l\ P_{jl}.\ |^2, \qquad \text{(B-12)}$$

where $\eta = \boldsymbol{h}/h$ and $|\eta\ |^2=1$.

In order to sum up the contribution from equivalent orientations, the product $P_{ij}P_{kl}$ of the dipole tensors over all possible orientations have to be averaged. For cubic crystals it can be written in the form

$$<P_{ij}P_{kl}> = \Pi^{(1)}\delta_{ij}\delta_{kl}/3 + \Pi^{(2)}(\delta_{ijkl} - \delta_{ij}\delta_{kl}/3)$$
$$+ \Pi^{(3)}\{(\delta_{ik}\delta_{jl} + \delta_{il}\delta_{jk})/2 - \delta_{ijkl}\} \qquad \text{(B-13)}$$

with

$$\delta_{ijkl} = \{\ 1\ (i=j=k=l)\ ,\ 0\ \text{(otherwise)}\ \}\ , \qquad \text{(B-14)}$$
$$\Pi^{(1)} = (1/3)(P_{11}+P_{22}+P_{33})^2\ ,$$
$$\Pi^{(2)} = (1/6)\{(P_{11}-P_{22})^2+(P_{22}-P_{33})^2+(P_{33}-P_{11})^2\}\ ,$$
$$\Pi^{(3)} = (2/3)(P_{12}^2+P_{23}^2+P_{31}^2)\ ,$$

where $\Pi^{(1)}$ is the contribution from the volume change, $\Pi^{(2)}$ is from the shear, $\Pi^{(3)}$ is from the rotation. Thus the average of the Huang scattering intensities over all possible orientations are obtained by

$$S_{\text{Huang}}(\boldsymbol{K}) = cN\ |f\ |^2(h/qV_c)^2\ (\gamma^{(1)}(\kappa)\Pi^{(1)} + \gamma^{(2)}(\kappa)\Pi^{(2)} + \gamma^{(3)}(\kappa)\Pi^{(3)}), \qquad \text{(B-15)}$$

with

$$\gamma^{(1)}(\kappa) = (T_{11}+T_{22}+T_{33})^2/3,$$
$$\gamma^{(2)}(\kappa) = \{(T_{11}-T_{22})^2+(T_{22}-T_{33})^2+(T_{33}-T_{11})^2\}/3,$$
$$\gamma^{(3)}(\kappa) = \{(T_{11}+T_{22})^2+(T_{22}+T_{33})^2+(T_{33}+T_{11})^2\}/2,$$
$$T_{ij} = \Sigma_l\eta_l\zeta_{li}(\kappa)\kappa_j.$$

When the scattering is limited on the (hk0) plane, κ_{33} and T_{33} become zero, and

$$\gamma^{(1)} = (1/3)(T_{11}^2+T_{22}^2+2T_{11}T_{22})$$

$$\gamma^{(2)} = (2/3)(T_{11}^2+T_{22}^2-T_{11}T_{22}).$$

First, let us consider the tetragonal defect. The dipole tensor P_{ij} is defined as $P_{11}=P_{22}=-1$, $P_{33}=2$, $P_{ij}=0$ $(i \neq j)$. Then, $\Pi^{(1)}=\Pi^{(3)}=0$, $\Pi^{(2)}=3$ and

$$S_{\mathrm{Huang}}(\boldsymbol{K}) = 2cN\,|f|^2(h/qV_c)^2(T_{11}^2+T_{22}^2-T_{11}T_{22}). \tag{B-16}$$

We put the unit vector of the deviation from Bragg point:

$$\eta = (\eta_1,\eta_2,0)$$

then T_{11} and T_{22} become

$$T_{11} = \eta_1\zeta_{11}(\kappa)\kappa_1 + \eta_2\zeta_{21}(\kappa)\kappa_1 \ , \tag{B-17}$$

$$T_{22} = \eta_1\zeta_{12}(\kappa)\kappa_2 + \eta_2\zeta_{22}(\kappa)\kappa_2 \ .$$

From the definition of $\zeta_{ij}(\kappa)$, they can be calculated as the inverse of this matrix:

$$\zeta_{ij} = \begin{pmatrix} c_{11}\kappa_1^2 + c_{44}\kappa_2^2 & (c_{11}+c_{44})\kappa_1^2\kappa_2^2 & 0 \\ (c_{11}+c_{44})\kappa_1^2\kappa_2^2 & c_{11}\kappa_1^2 + c_{44}\kappa_2^2 & 0 \\ 0 & 0 & c_{44}(\kappa_1^2+\kappa_2^2) \end{pmatrix}^{-1} . \tag{B-18}$$

Acknowledgements

The author would like to express his sincere thanks to Prof.Y.Yamada of Institute of Solid State Physics for his helpful guidance throughout this study and to Dr.Y.Noda of Osaka University for his instructions about the experiments and discussions. The author also thanks Dr.M.Sato of Institute for Molecular Science and Mr.T.Kitazawa of Institute of Solid State Physics for giving advice regarding preparation of the samples, and thanks Prof.F.E.Fujita, Dr.R.Ohshima, Dr.K.Fuchizaki of Osaka University, Prof.Y.Fujii of Tsukuba University and Prof.Y.Ishibashi of Nagoya University for valuable discussions.

References

1) Y.Yamada: Structural phase transition and neutron scattering. *Butsurigaku Saizensen.***6** (1984) 129 (*in Japanese*).

2) C.M.Hwang, M.Meichle, M.B.Salamon and C.M.Wayman: J. de Phys. **43** (1982) c4-231.

3) T.Suzuki, M.Takagi, A.Nagasawa and N.Nakanishi: J. Mat. Sci. **16** (1981) 3013.

4) G.D.Sandrock, A.J.Perkins and R.F.Heheman: Metall. Trans. **2** (1971) 2769.

5) A.Nagasawa: J. Phys. Soc. Jpn. **40** (1976) 93.

6) P.Moine, G.M.Michal and R.Sinclair: Acta Metall. **30** (1982) 109.

7) R.Ohshima and M.Sugiyama: J. de Phys. **43** (1982) c4-383.

8) L.Delaey, A.J.Perkins and T.B.Massalski: J. Mat. Sci. **7** (1972) 1197.

9) L.Delaey, P.F.Goblin, G.Guenin and H.Warlimont: *Proc ICOMAT-79, Chambridge*, MA, MIT, (1979) 400.

10) L.E.Tanner, A.R.Pelton and R.Gronsky: J. de Phys. **43** (1982) c4-169.

11) J.D.C.McConell: American Mineralogist, **68** (1983) 1.

12) H.Boehm: American Mineralogist, **68** (1983) 11.

13) A.H.Heuer and M.Ruehle: Acta Metall. **33** (1985) 2101.

14) H.Bestgen: Solid State Comm. **58** (1986) 197.

15) M.Mori, Y.Noda and Y.Yamada: J. Phys. Soc. Jpn. **48** (1980) 1288.

16) J.D.C.McConnell and V.Heine: J. Phys. **C15** (1982) 2387.

17) E.Fawcett: Phys. Rev. Lett. **26** (1971) 829.

18) G.R.Barsch and Z.P.Chang: Phys. Rev. **B24** (1981) 96.

19) T.Onozuka, N.Ohnishi and M.Hirabayashi: Metall. Trans. **19A** (1988) 797.

20) M.Milewits and S.J.Williamson: J. de Phys. **39** (1978) c6-408.

21) M.B.Salamon, M.Meichle, C.M.Wayman, C.M.Hwang and S.M.Shapiro: *AIP Proc.* **53** (1979) 223.

22) S.M.Shapiro, Y.Noda, Y.Fujii and Y.Yamada: Phys. Rev. **B30** (1984) 4314.

23) Y.Noda, M.Takimoto, T.Nakagawa and Y.Yamada: Metall. Trans. **19A** (1988) 265.

24) Y.Yamada: *Proc. ICOMAT-86* (1986) 89.

25) Y.Yamada: Metall. Trans. **19A** (1988) 777.

26) Y.Yamada, Y.Noda, M.Takimoto and K.Furukawa: J. Phys. Soc. Jpn. 54 (1985) 2940.

27) Y.Yamada, Y.Noda and M.Takimoto: Solid State Comm. 55 (1985) 1003.

28) K.Fuchizaki, Y.Noda and Y.Yamada: to be published in Phys. Rev B.

29) M.Matui, H.Yamada and K.Adachi: J. Phys. Soc. Jpn. **48** (1980) 2161.

30) T.Sohmura, R.Ohshima and F.E.Fujita: Scripta Metall. **14** (1980) 855.

31) O.Nittono, H.Iwasaki and Y.Koyama: J. Jpn. Inst. Met. **44** (1980) 899 (*in Japanese*).

32) K.Shimizu, Y.Okamura and H.Kubo: Trans. Jpn. Inst. Met. **23** (1982) 53.

33) M.Sugiyama, R.Ohshima and F.E.Fujita: Trans. Jpn. Inst. Met. **27** (1986) 719.

34) R.Ohshima, M.Sugiyama and F.E.Fujita: Metall. Trans. **19A** (1988) 803.

35) M.Sato, B.H.Grier, S.M.Shapiro and H.Miyajima: J. Phys. **F12**(1982) 2117.

36) M.Sugiyama, S.Harada and R.Ohshima: Scripta Metall. **19** (1985) 315.

37) H.Seto, Y.Noda and Y.Yamada: J. Phys. Soc. Jpn. **57** (1988) 3668.

38) Y.Yamada: J. Cryst. Soc. Jpn. **22** (1980) 301 (*in Japanese*).

39) Y.Noda, M.Mori and Y.Yamada: J. Phys. Soc. Jpn. **45** (1978) 954.

40) Y.Yamada, M.Mori and Y.Noda: Solid State Comm. **32** (1979) 827.

41) K.Chiba, K.Suzuki and S.Chikazumi: J. Phys. Soc. Jpn. **39** (1975) 839.

42) S.M.Shapiro, M.Iizumi and G.Shirane: Phys. Rev. **B14** (1976) 200.

43) W.L.McMillan: Phys. Rev. **B14** (1976) 1496.

44) G.R.Barsch, J.A.Krumhansl, L.E.Tanner and M.Wuttig: Scripta Metall. **21** (1987) 1257.

45) F.Falk: Z. Physik **B51** (1983) 177.

46) G.R.Barsch and J.A.Krumhansl: Metall Trans. **19A** (1988) 761.

47) E.Pytte and J.Feder: Phys. Rev. **187** (1969) 1077.

48) M.Kataoka and J.Kanamori: J. Phys. Soc. Jpn. **32** (1972) 113.

49) J.D.Axe and Y.Yamada: Phys. Rev. **B24** (1981) 2567.

50) G.R.Barsch and J.A.Krumhansl: Phys. Rev. Lett. **53** (1984) 1069.

51) Y.Ishibashi and V.Dovorak: J. Phys. Soc. Jpn. **44** (1978) 32.

52) H.Shiba and Y.Ishibashi: J. Phys. Soc. Jpn. **44** (1978) 1592.

53) Y.Ishibashi, J.Sugiyama and A.Sawada: J.Phys. Soc. Jpn. **50** (1981) 2500.

54) P.H.Dederichs: J. Phys. **F3** (1973) 471.

55) G.R.Barsch: *unpublished work.*

56) P.H.Dederichs: Phys. Rev. **188** (1969) 1175.

(a) T>Tc

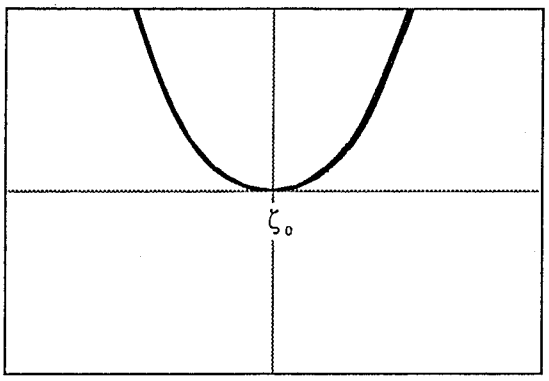

(b) T=Tc

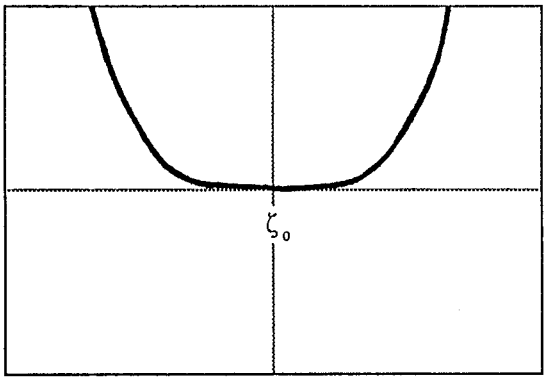

(c) T<Tc

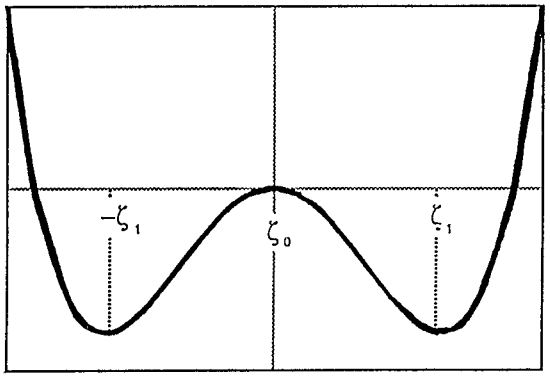

Fig.1-1 Schematic representation of temperature variation of the potential curve in second order phase transitions. The Horizontal axis ζ indicates the order parameter. The values ζ_0 and $\pm\zeta_1$ correspond to the order parameters in the high and low temperature phase, respectively.

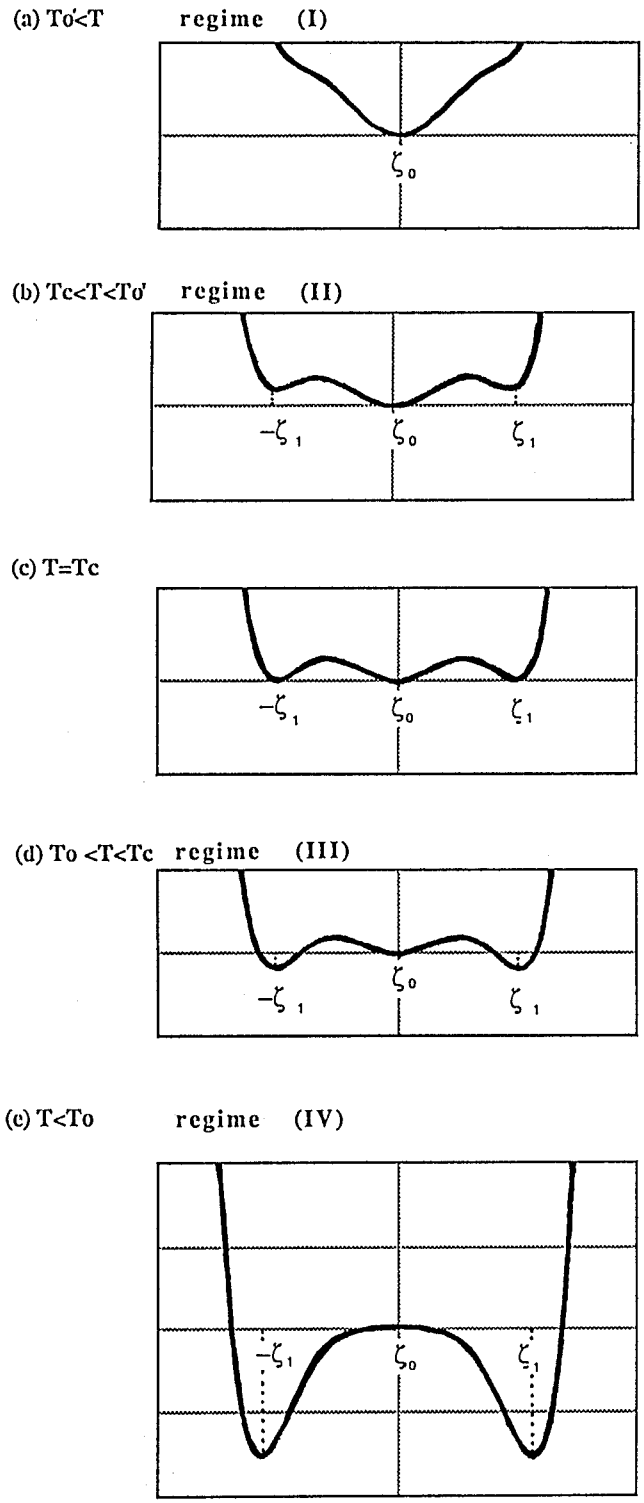

Fig.1-2 Schematic representation of the temperature variation of the potential curve around the first order phase transition point. We divide the temperature region into four regimes. (See the text.) (a) $T>T_0'$ (regime (I)), (b) $T_c<T<T_0'$ (regime (II)), (c) $T=T_c$ (transition point), (d) $T_0<T<T_c$; (regime (III)), (IV) $T<T_0$ (regime (IV)).

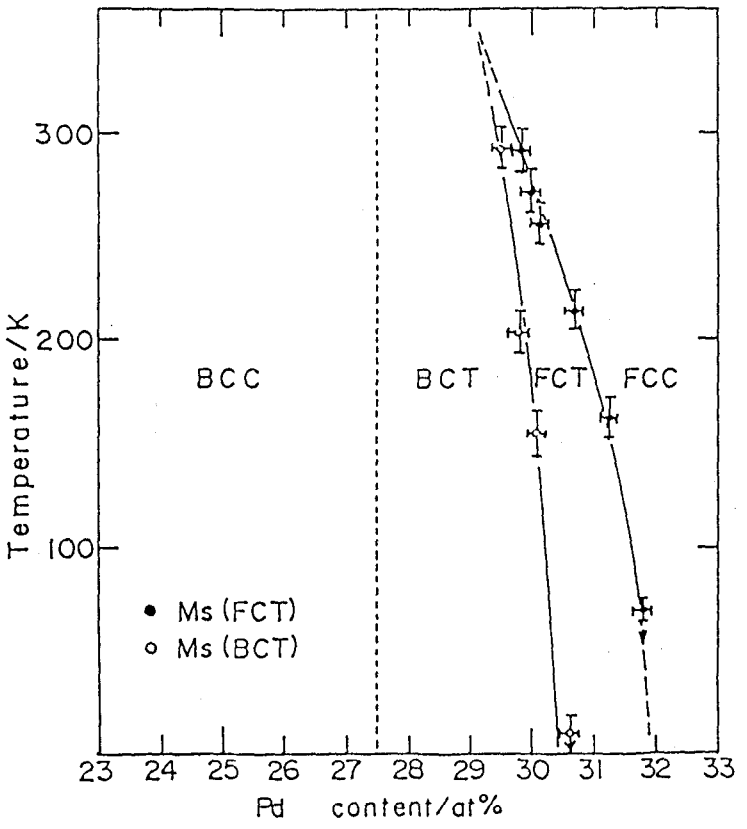

Fig.1-3 Phase diagram of $Fe_{1-x}Pd_x$ system determined by Sugiyama *et al.*[33]
In the narrow concentration range of $0.29 \leq x \leq 0.32$ the system undergoes martensitic fcc-fct transformation.

(a)

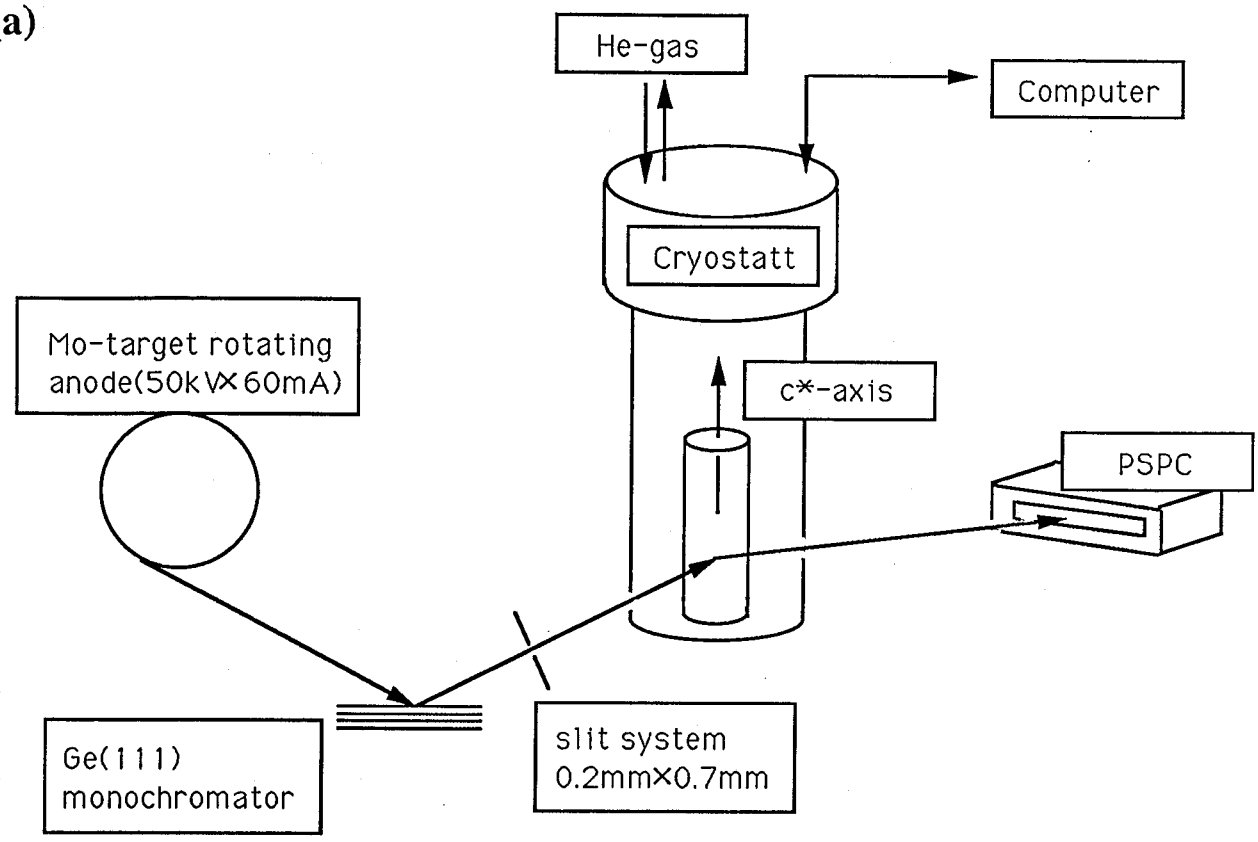

(b)

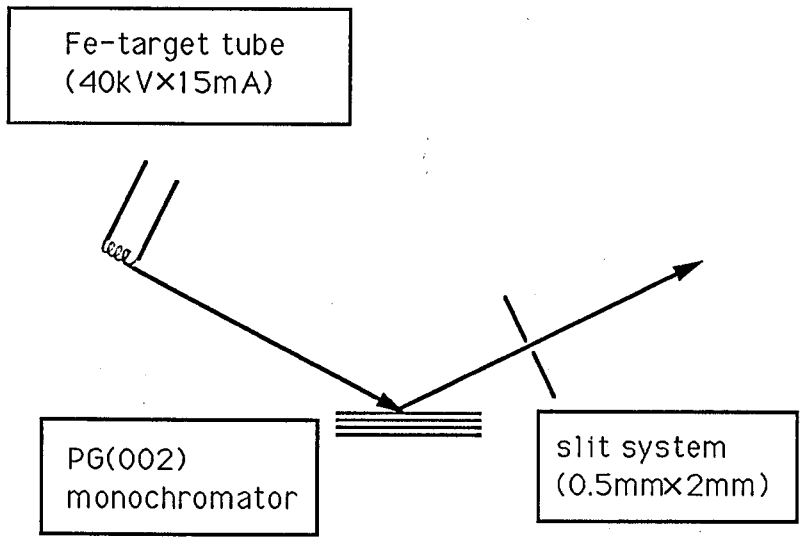

Fig.2-2-1 Schematic representations of the X-ray diffraction instruments; (a) high resolution type, (b) low resolution type.

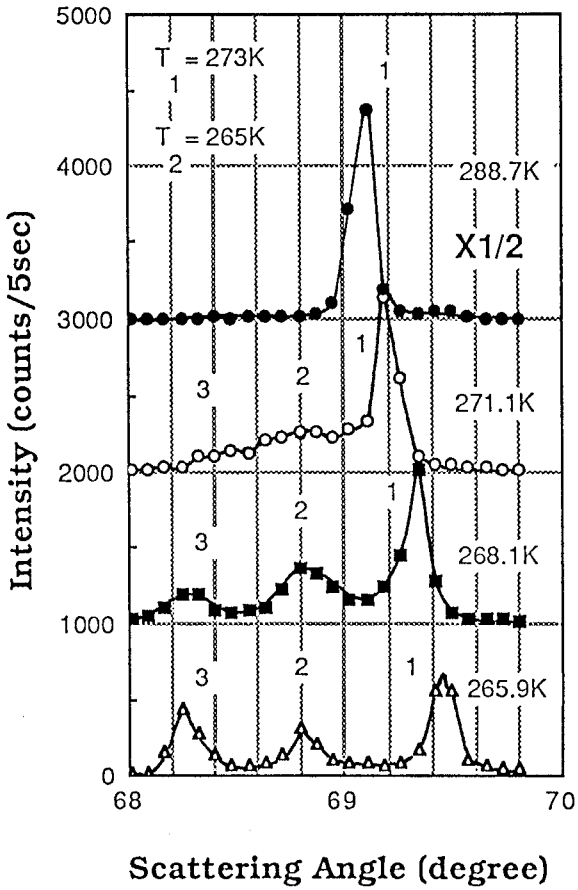

Fig.2-2-2 Temperature variation of the peak profile around the (600) Bragg point in the intermediate phase. In this temperature region, the peak position remains on the line of the [100] direction. The horizontal axis indicates the [100] direction by values of 2θ.

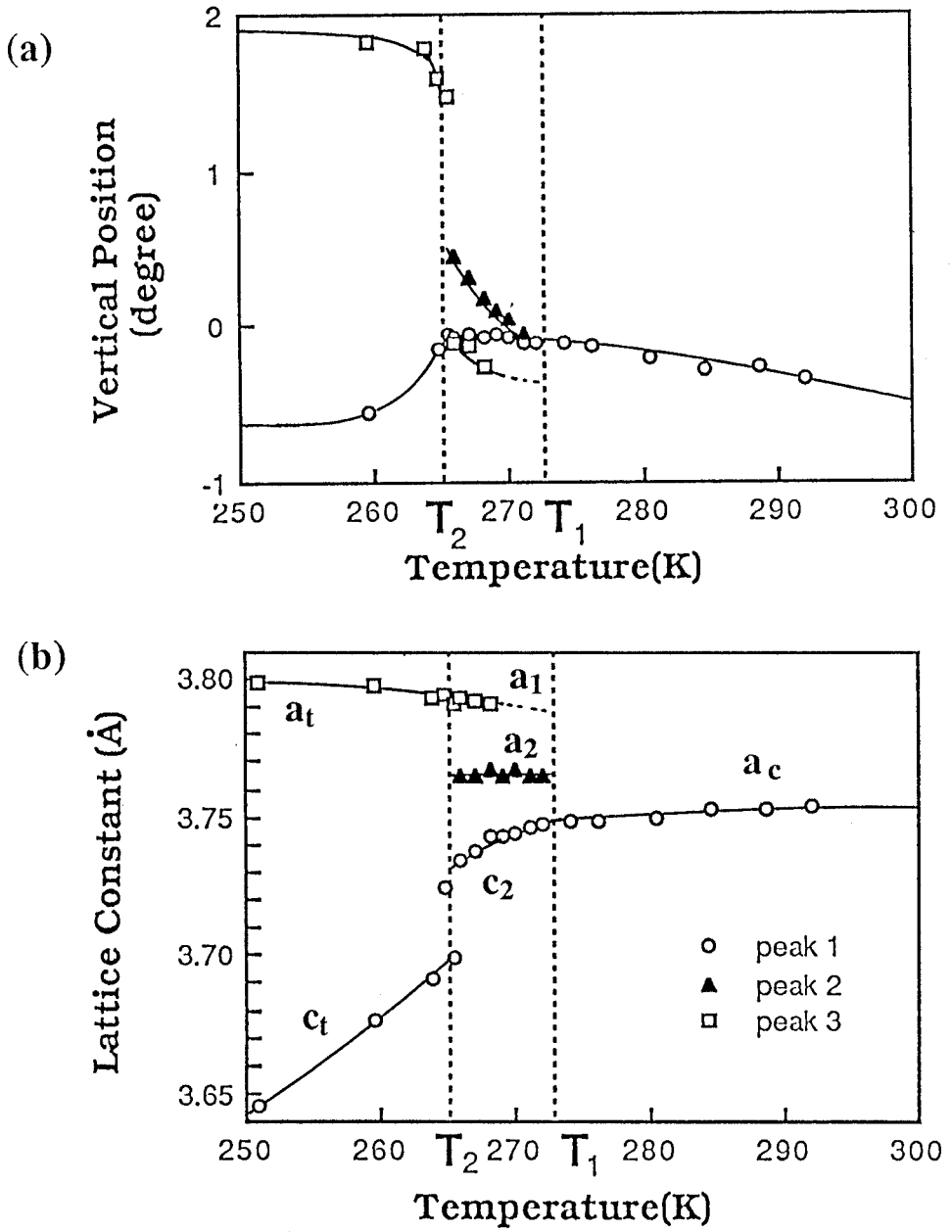

Fig.2-2-3 (a) Temperature dependence of the deviation of (600) Bragg peak in the direction perpendicular to the scattering plane. It was measured by setting the position sensitive proportional counter vertically. (b) Temperature dependence of the lattice constants calculated from the peak positions around the (600) Bragg point. Two phase transition points on cooling are defined as T_1=273K and T_2=265K. Peak 3 becomes too weak around T_1 to be identified. Since the irradiated grain did not include the lattice with parameter c_1, the lattice constant c_1 was not observed. (See the text.) Because of the small hysteresis at the lower temperature phase transition, the peak corresponding to c_t exists just above T_2.

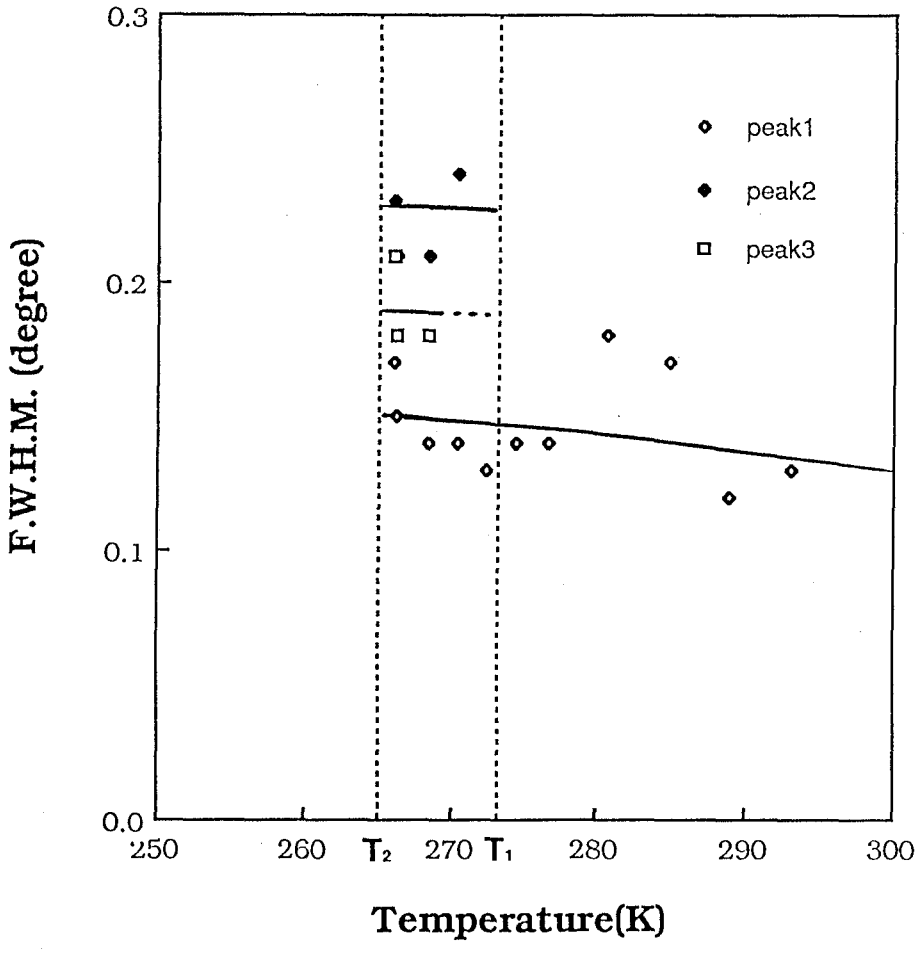

Fig.2-2-4 Temperature dependence of the full-width-at-the-half-maximum (FWHM) of each peak. Appreciable broadening of the profiles in the intermediate temperature region was not observed. Because the peaks moved off from the scattering plane below T_2, it was difficult to discuss the width precisely.

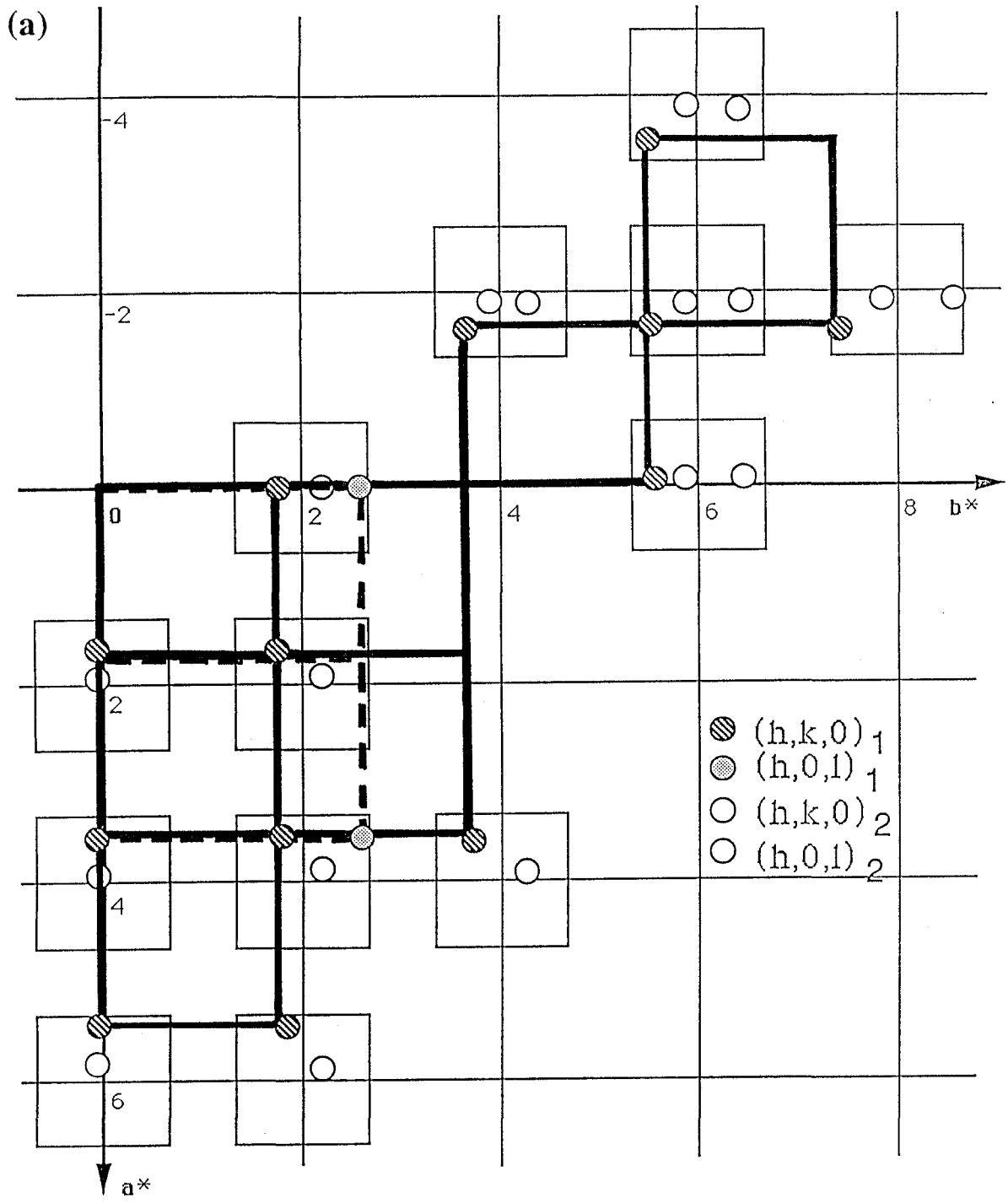

Fig.2-2-5 Schematic representation of a part of the observed splitting of Bragg peaks at 267.5K (intermediate phase). Thin solid lines represent the original cubic lattice. The amounts of the shifts are magnified by factor 10 in the square region around each Bragg position. Of the total of 44 observed split points, only 33 points are included in the figure. One of the set of the tetragonal lattice is represented by thick lines in (a), and the other set is given in (b). All of the peaks can be indexed assuming these two tetragonal lattices.

(b)

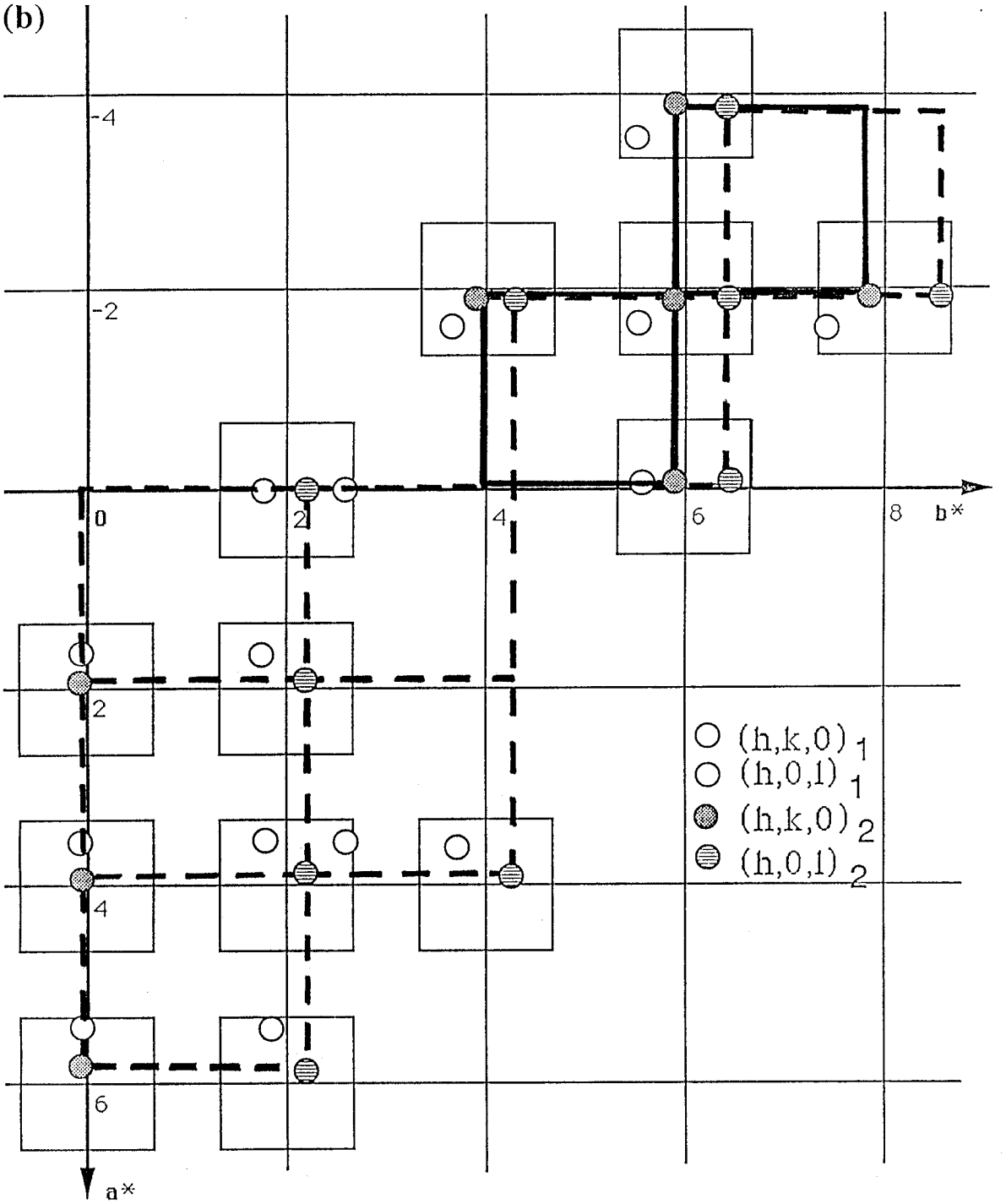

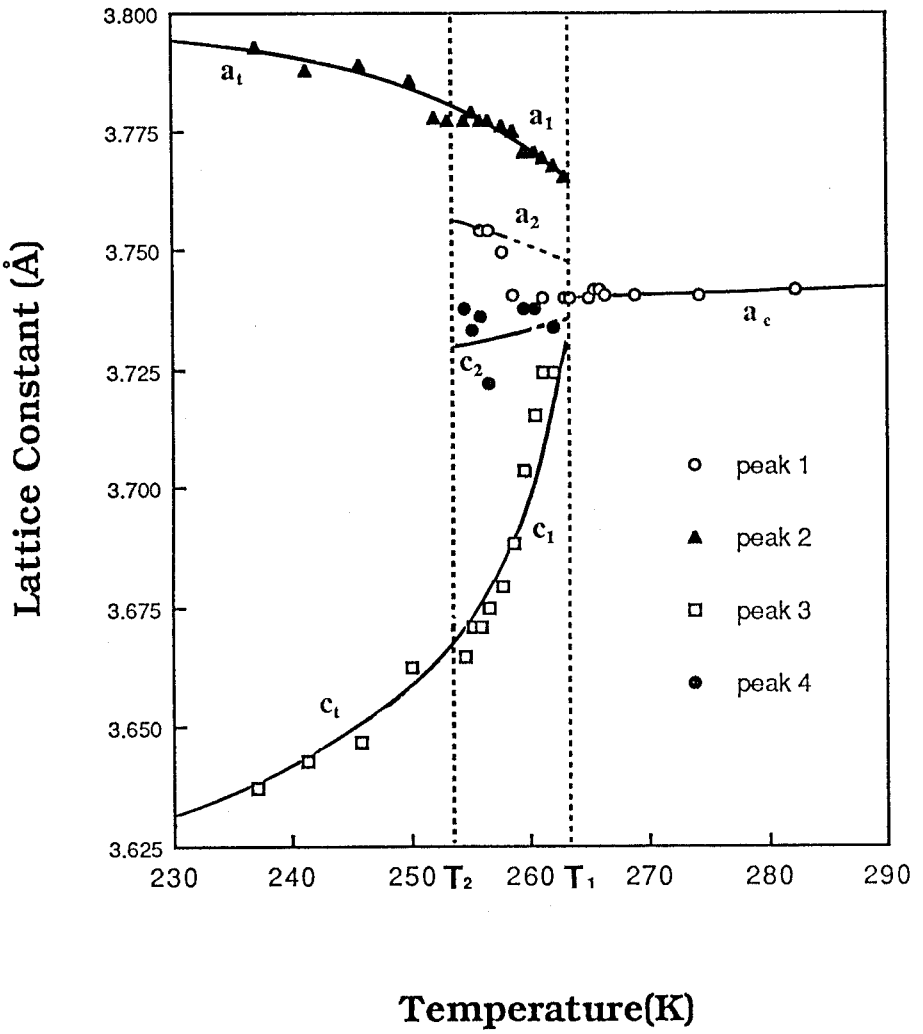

Fig.2-2-6 Temperature dependence of the lattice constants calculated from the peak positions around the (200) Bragg point for the crystal containing 30.2 at%-Pd. Two transition temperatures are determined as T_1=263K and T_2=253K. Because the instrumental resolution was poor as compared with the high resolution experiments, the peak splitting of peak 1 and 4 was not very clear to identify the peak positions just below T_1, but the broadening of the peak to the θ-2θ direction caused by the small splitting is seen. Just above T_2, we could identify four peaks so that the existence of the two tetragonal lattices was established.

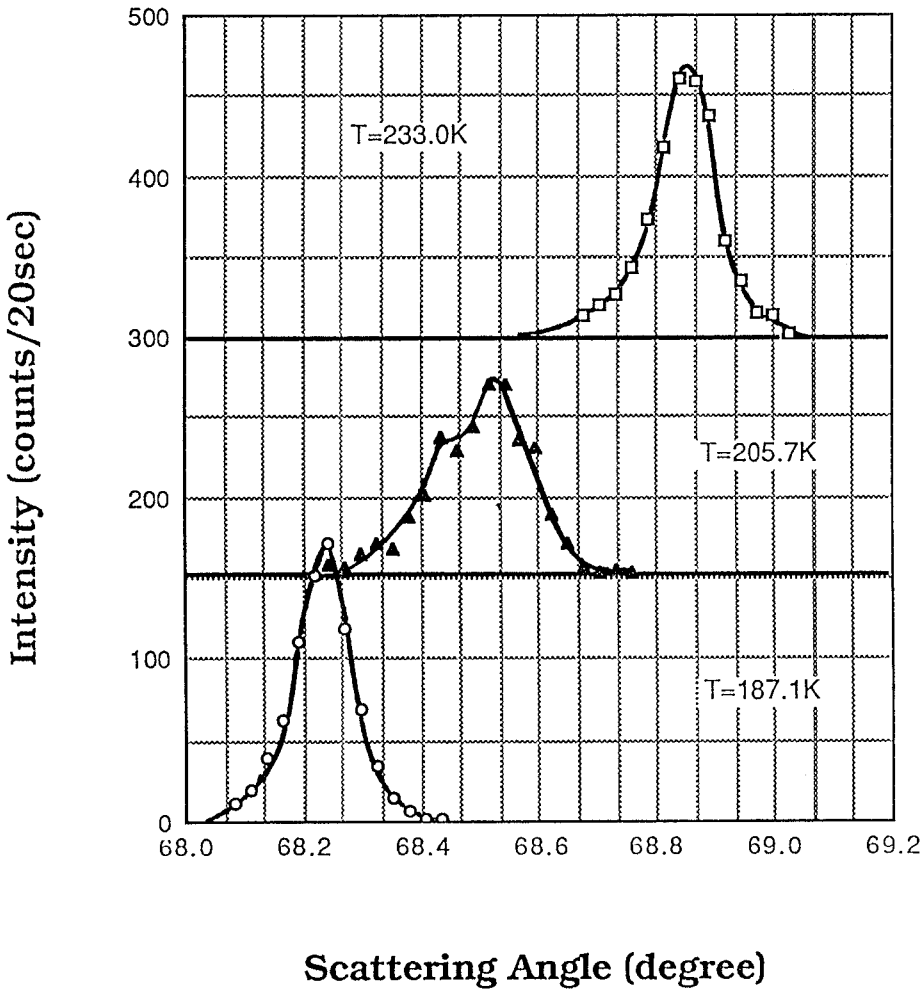

Fig.2-2-7 Temperature variation of the (600) peak profile for the crystal containing 31.2 at%-Pd around the intermediate phase. The horizontal axis indicate the value of the scattering angle. The upper profile shows the high temperature fcc phase, and the lower one applies the (600) reflection of the 'pure' fct phase. The Broadening of the one in middle is caused by the slight splitting in the intermediate phase.

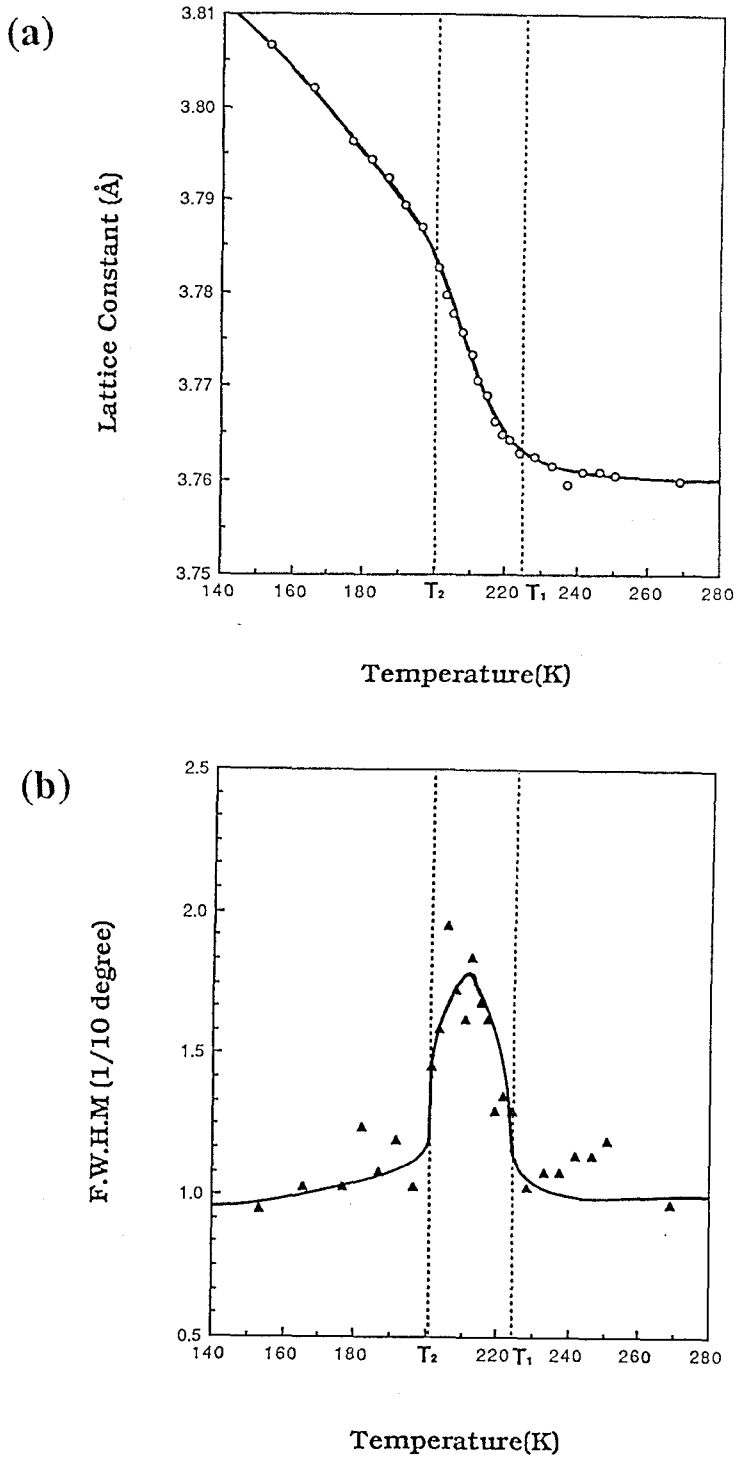

Fig.2-2-8 (a) Temperature dependence of the lattice constant calculated from the (600) Bragg peak position in the sample nominally containing 31.2 at%-Pd. (b) Temperature dependence of the line width of (600) peak. From the temperature range of the broadening, we can determine the two transition temperature: T_1=224K, T_2=201K.

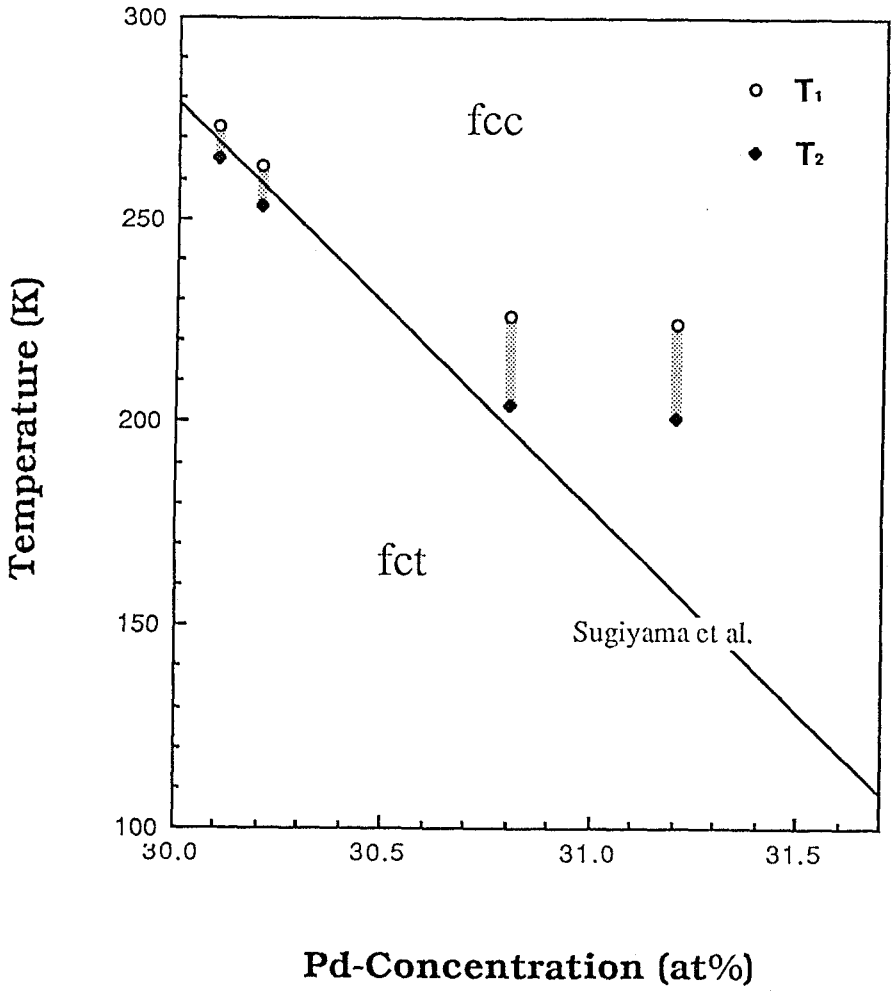

Fig.2-2-9 Phase diagram obtained by the present experiments. The horizontal axis indicates the nominal palladium concentration. Error ranges of the actual concentration estimated from chemical analysis for the two higher concentration samples are about ±1 at%. The meshed lines between two transition points T_1 and T_2 indicate the ranges of the intermediate phase.

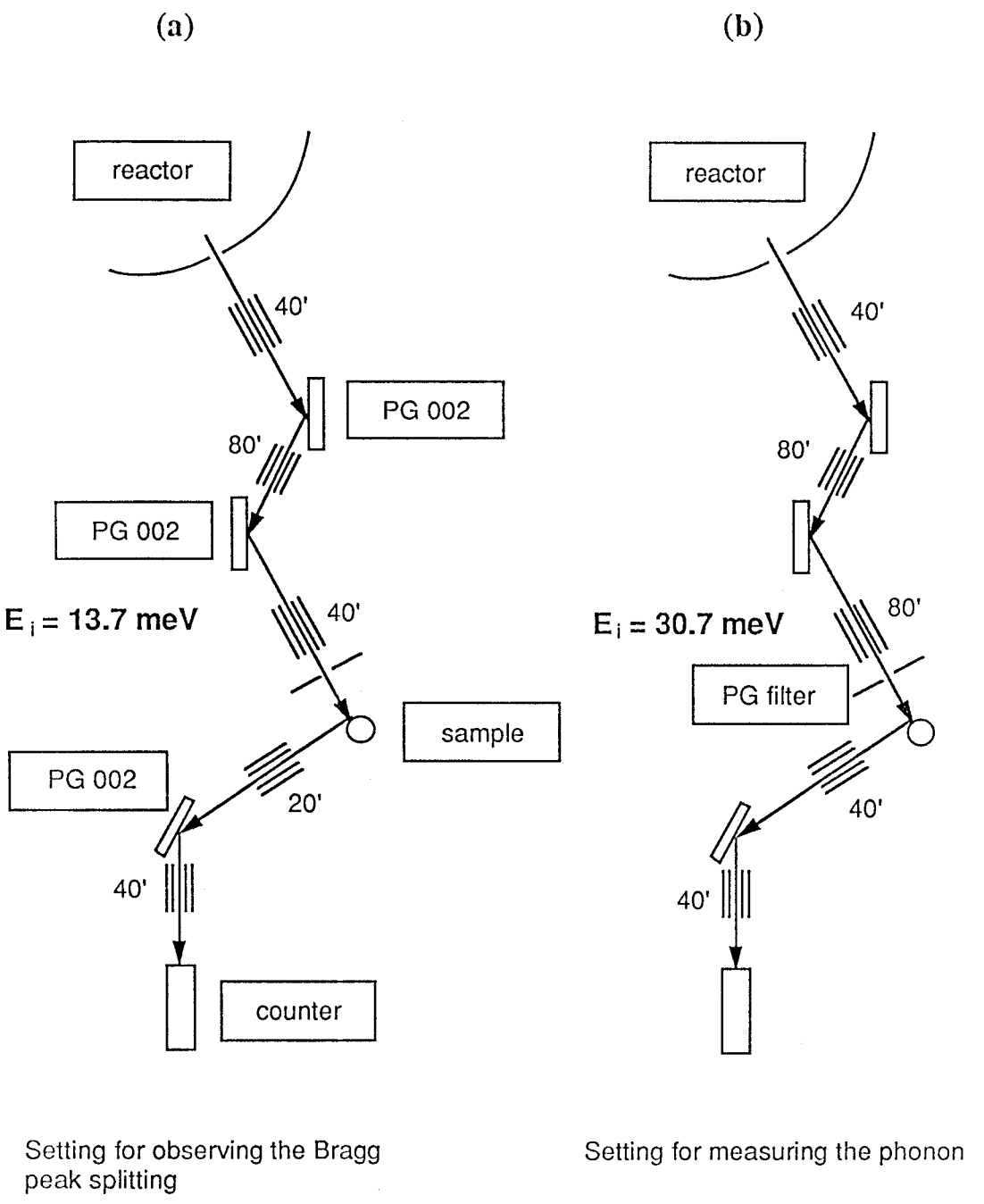

Fig.2-3-1 Schematic representations of the HT-8 triple axis diffractometer in JRR2, JAERI, TOKAI. (a) Setting for observing the Bragg peak splitting. The incident energy and the collimations were selected in order that a resolution is as high as possible. (b) Setting for measuring the phonon. The conditions were determined to observe phonons around (220) Bragg point.

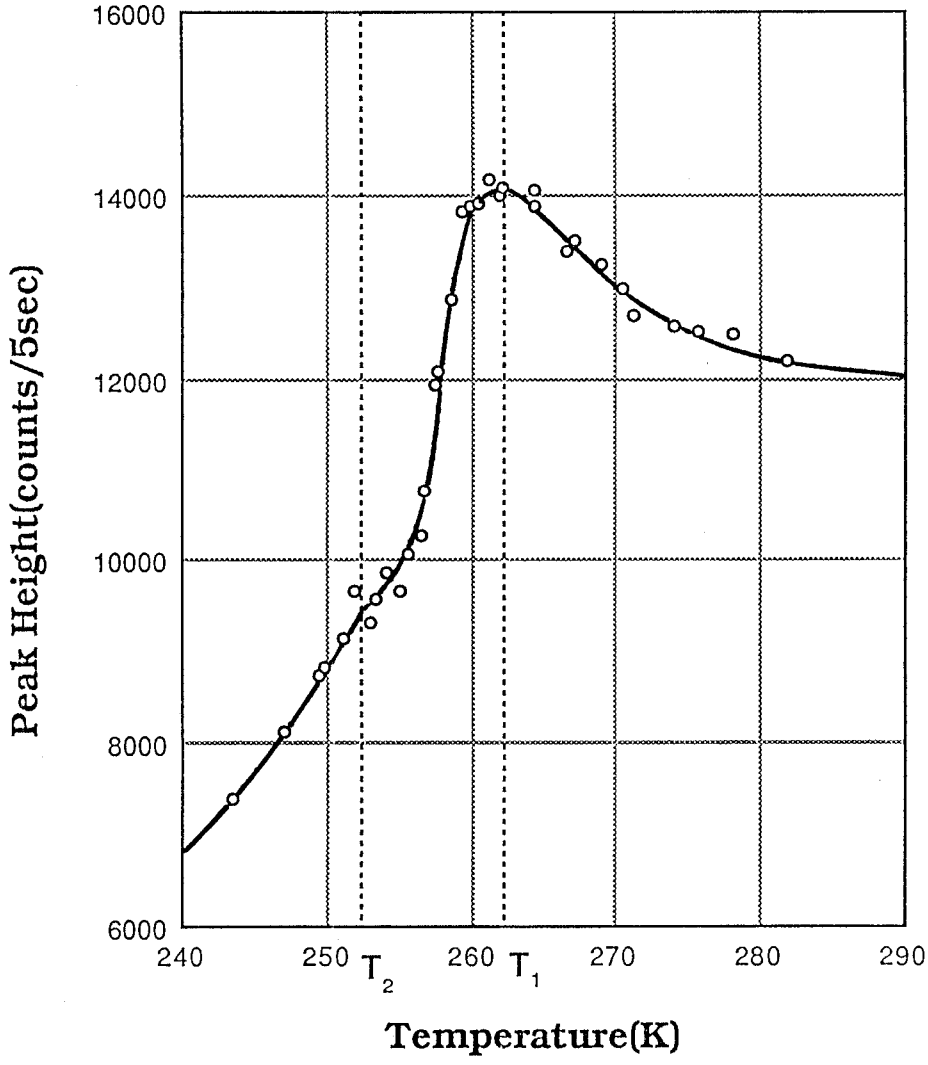

Fig.2-3-2 Temperature variation of the peak height of the (200) reflection for the sample containing 30.2 at%-Pd by neutron diffraction. The abrupt decrease at T_1 indicates the splitting of the peak in the intermediate phase. The two transition temperature T_1=263K and T_2=253K are consistent with the result of the X-ray diffraction.

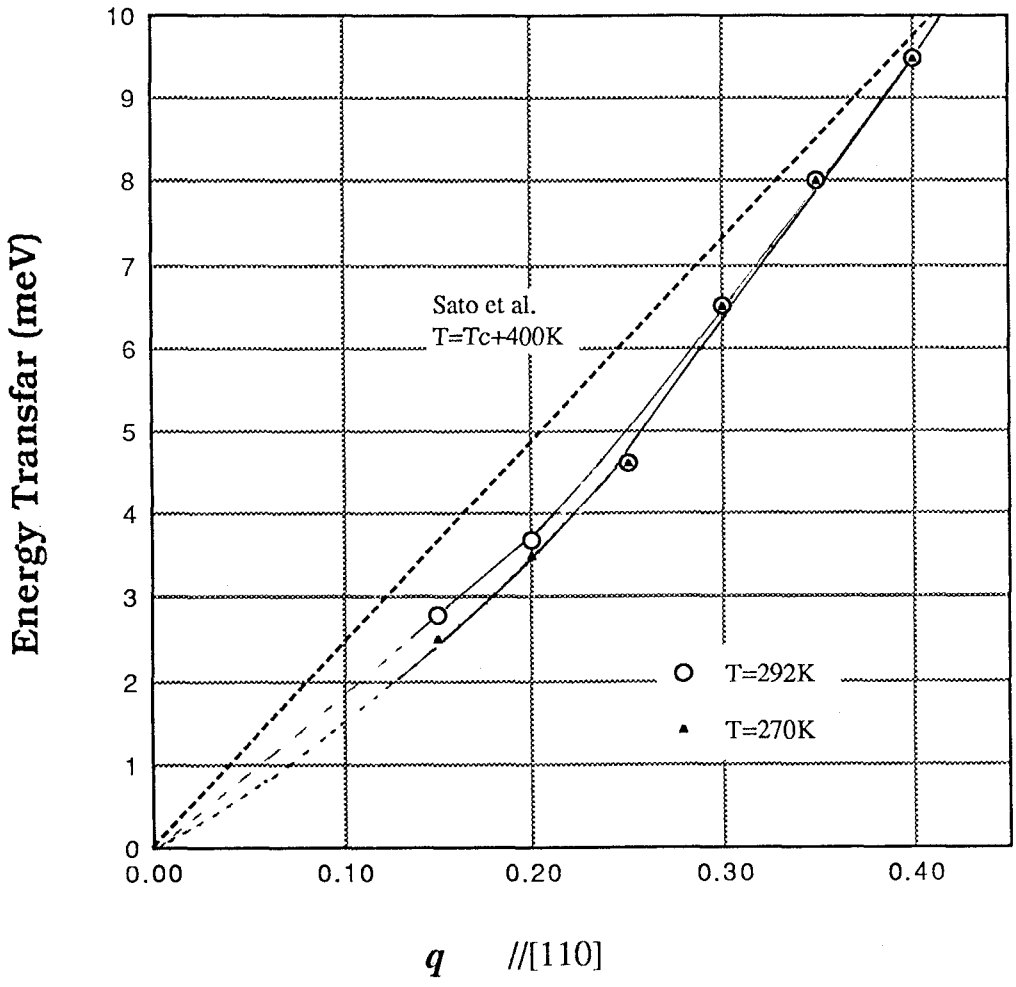

Fig.2-3-3 The dispersion curves in the direction of [110] measured by inelastic neutron scattering. The open chicles show the data at T_1+30K and the full triangles show the data at T_1+7K, just above the transition point. Dashed line observed by Sato *et al.* indicates the dispersion curve just below Curie point from which phonon softening starts. We could not observe appreciable softening of [110]TA phonon branch in this q-region.

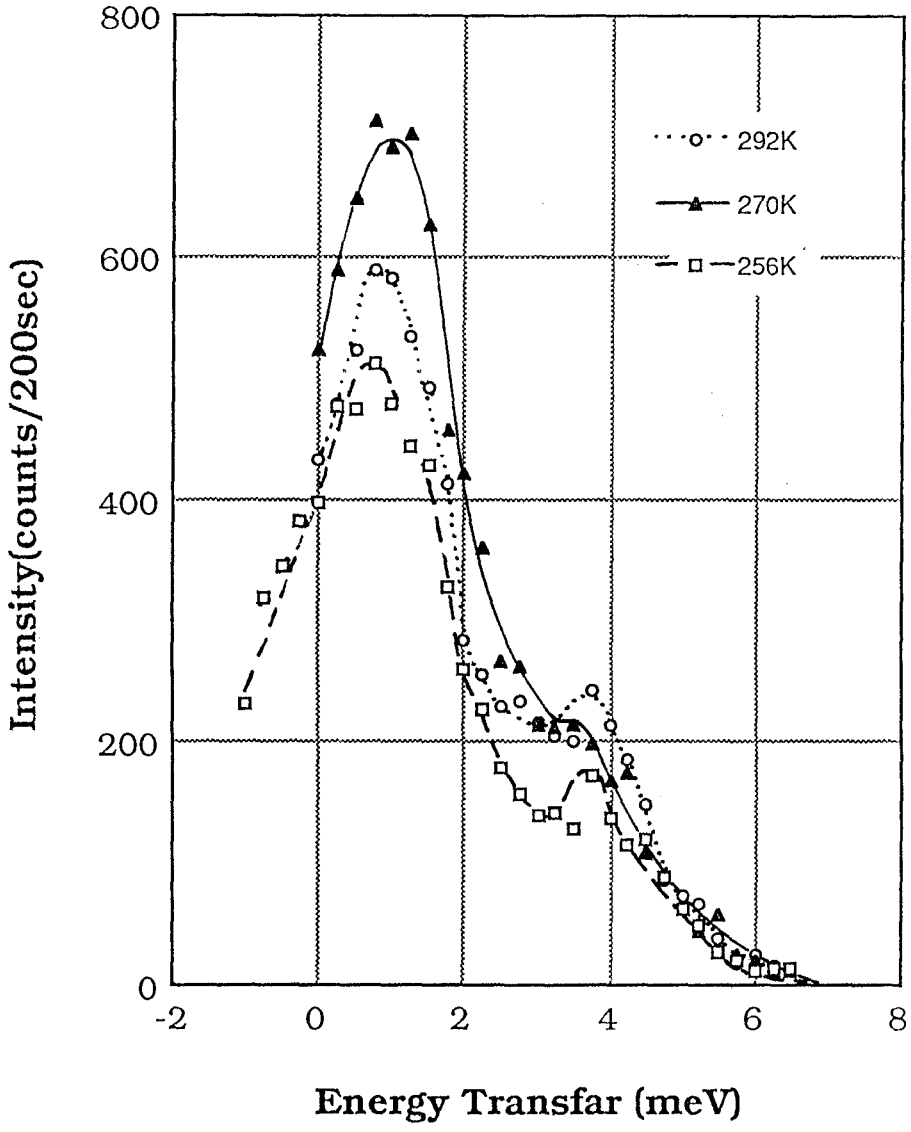

Fig.2-3-4 The temperature variation of the phonon spectra measured by constant-q scans (q=0.2). The open circles and dotted line indicate the data at T=292K, far above T_1, the full triangles and solid line at T=270K, just above T_1, and the open squares and dashed line at T=256K, in the intermediate phase. Instead of the phonon softening, the increase of the central mode (quasi-elastic component) were observed. The off-set of the peak position of the quasi-elastic scattering from E=0 is due to the effect of the oblique direction of the resolution function in the E-q plane.

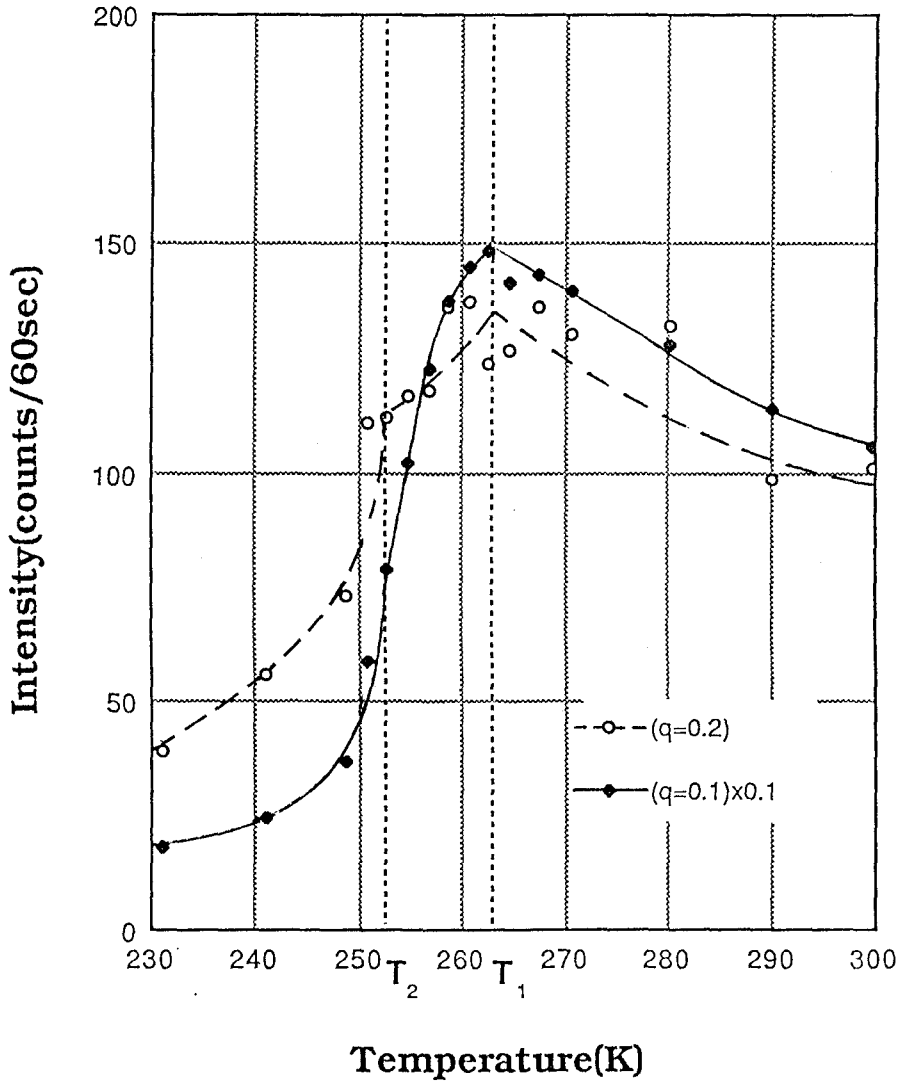

Fig.2-3-5 Temperature dependences of the intensity of the quasi-elastic scattering measured at (2.1,1.9,0) (the full circles and the solid line) and (2.2,1.8,0) (the open circles and the dashed line). The observed intensities at q=0.2 may be influenced by the phonons.

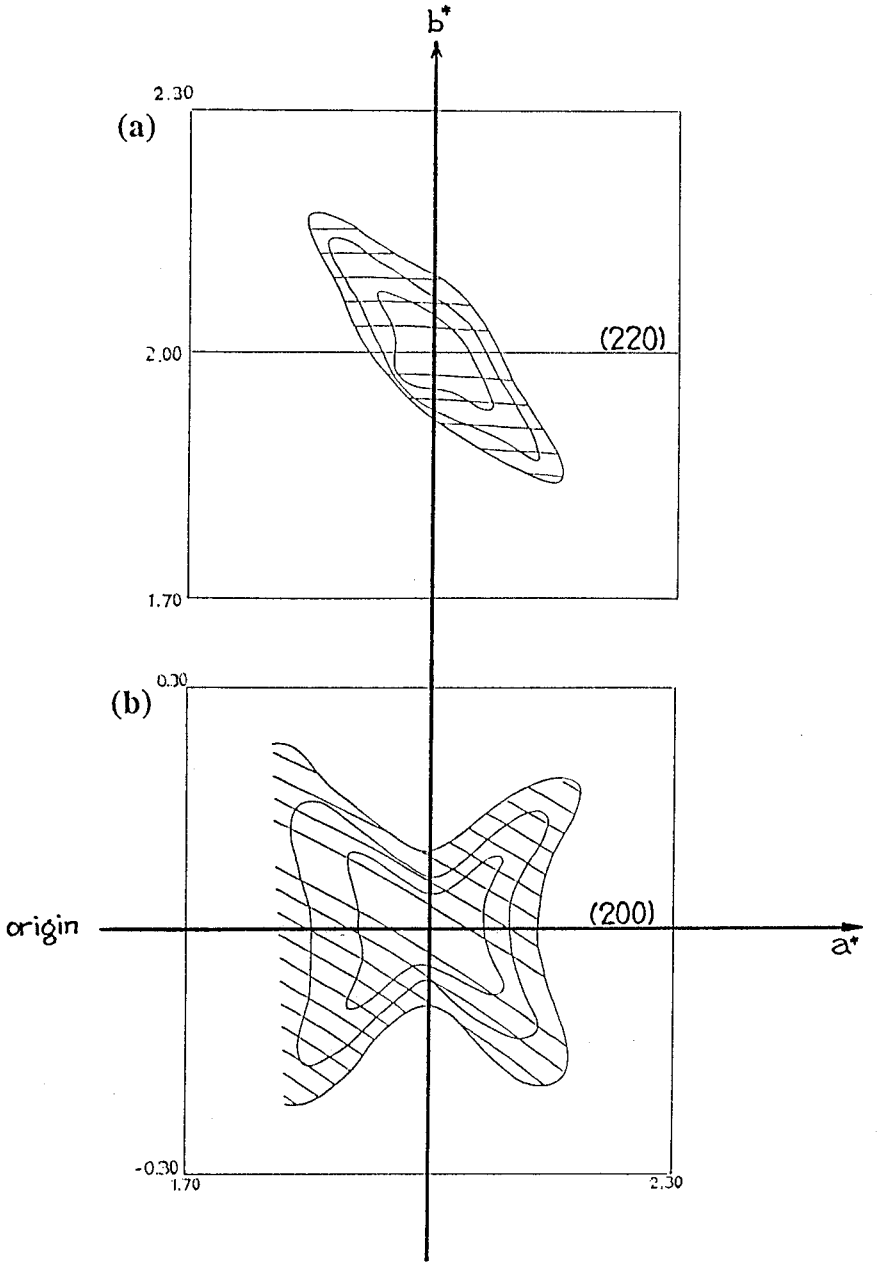

Fig.2-4-1 The intensity contours of the Huang diffuse scatterings observed by X-ray measurements for the sample nominally containing 31.6 at%-Pd whose features (such as real Pd concentration, transition temperature, etc.) has not been measured precisely. The diffuse intensities around (220) and (200) in (hk0) plane are shown in (a) and (b), respectively. The thin lines in the figures indicate the lines of the simultaneous observation by the position sensitive proportional counter. These profiles are the same in another crystals.

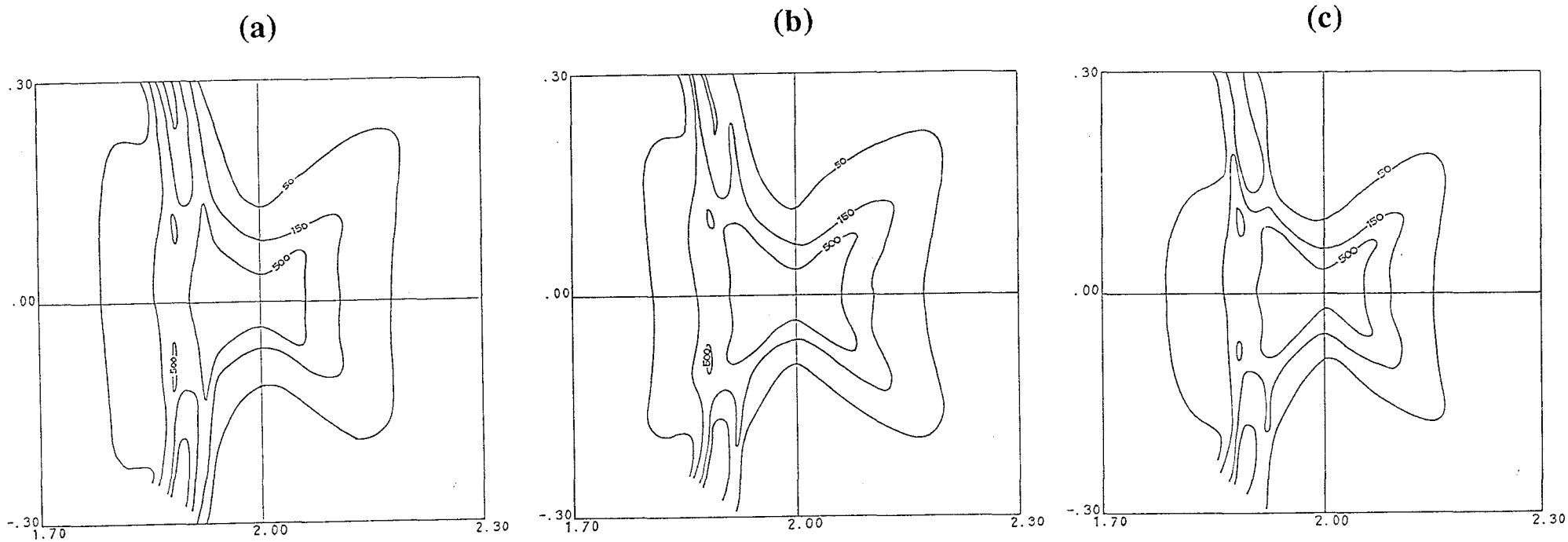

Fig.2-4-2 Intensity contours of the Huang diffuse scattering around the (200) Bragg point observed by X-ray measurements at various temperatures: (a) T=315K, far above the first transition temperature (T_1). (b) T=275K, just above T_1. (c) T=268K, in the intermediate phase. Narrow distributions running along the ω-direction are due to contamination of powder reflections. Huang scattering shows the characteristic feature that the intensity increases just above T_1 and then decrease below T_1.

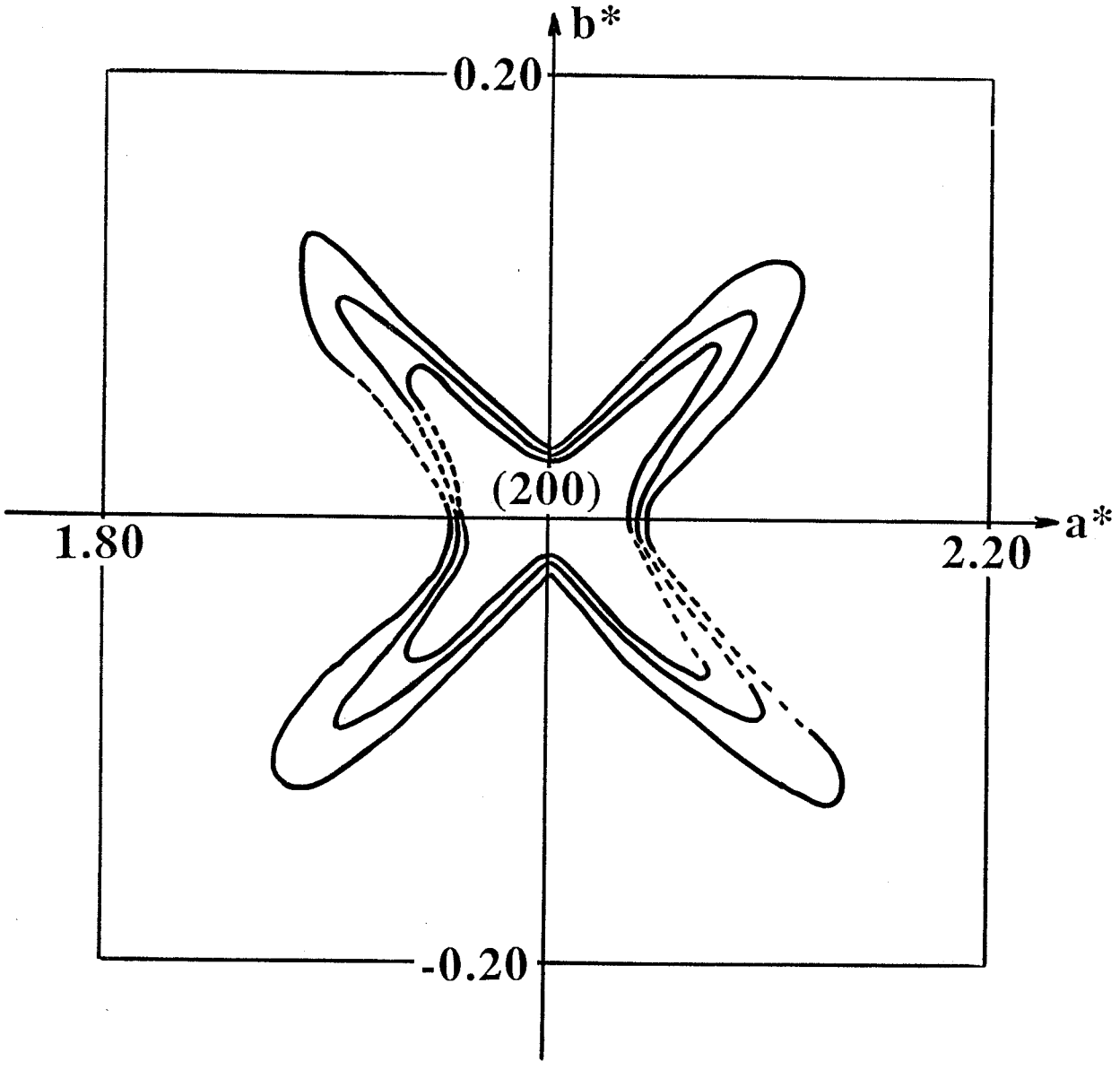

Fig.2-4-3 The intensity contour of the temperature dependent part of the Huang scattering, which is obtained by subtraction of the data at 315K (Fig.2-4-3 (a)) from the data at 275K (Fig.2-4-3 (b)). It is clearly seen that the sharp streaks are running in the direction of [110] and [$1\bar{1}0$], and it has the mirror symmetry around the plane perpendicular to the [100] direction.

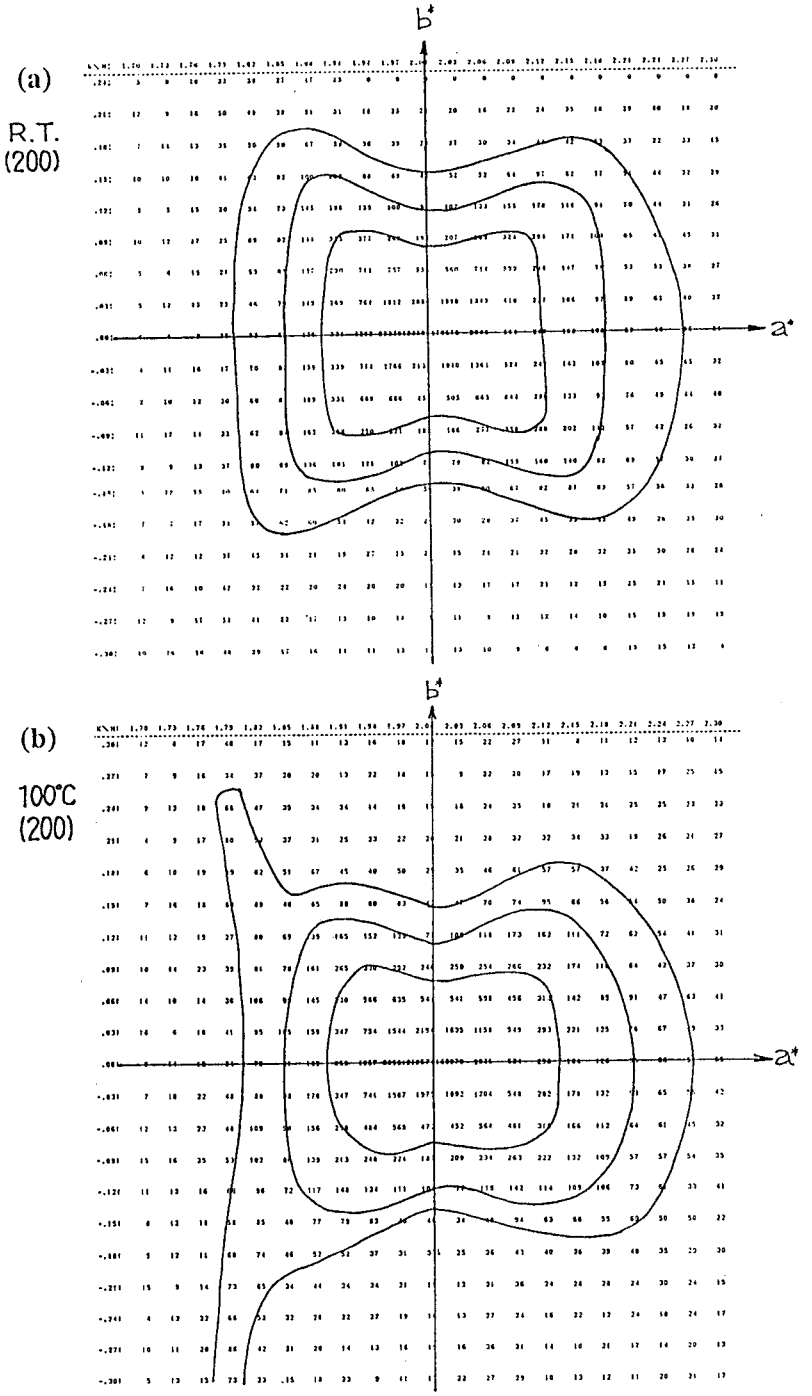

Fig.2-4-4 The intensity contours of the Huang diffuse scattering around (200) Bragg point obtained by the preliminary measurements with neutron scattering. The sample containing with 30.2 at%-Pd was used. The measurements were performed on the PANSI triple axis spectrometer at JRR2. Fixed incident energy of 41.0 meV was used and the collimations were selected as OPEN-20'-S-20'-A-60'. (a) T= T_1+30K, (b) T= T_1+110K. The diffuse intensities seem to extend to the [100] direction.

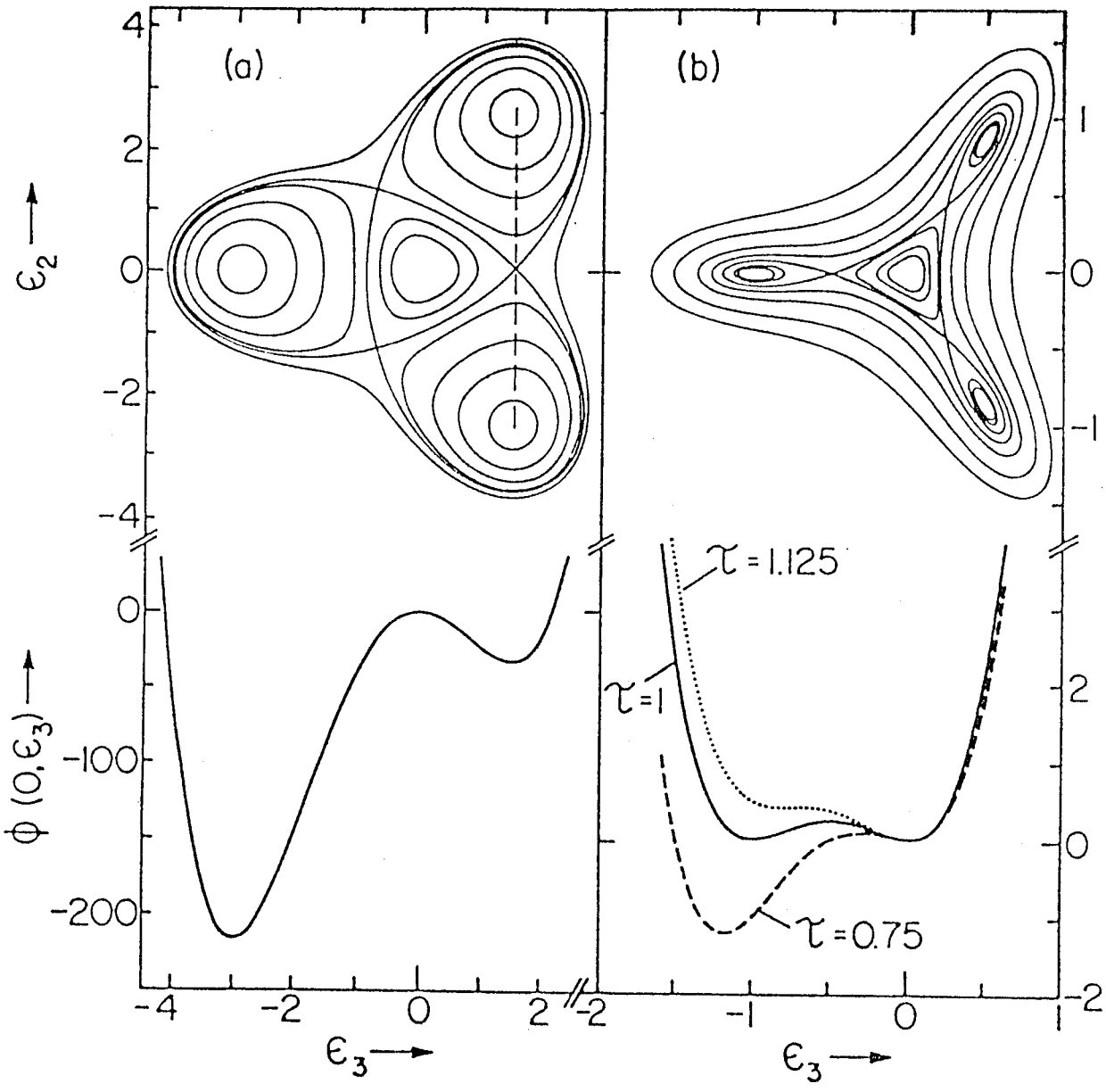

Fig.3-1 Curves of constant dimensionless strain energy $\phi(\varepsilon_2,\varepsilon_3) = \Phi(e_2,e_3)/\Phi_0 = \phi_0$, and section $\phi(0,\varepsilon_3)$ vs ε_3 with $\varepsilon_2 = e_2/e_0$, $\varepsilon_3 = e_3/e_0$, $e_0 = B/2C$, and $\Phi_0 = B^4/64C^3$. (a) For τ=-9. (b) For τ=1. (Fig.1 of ref.50.)

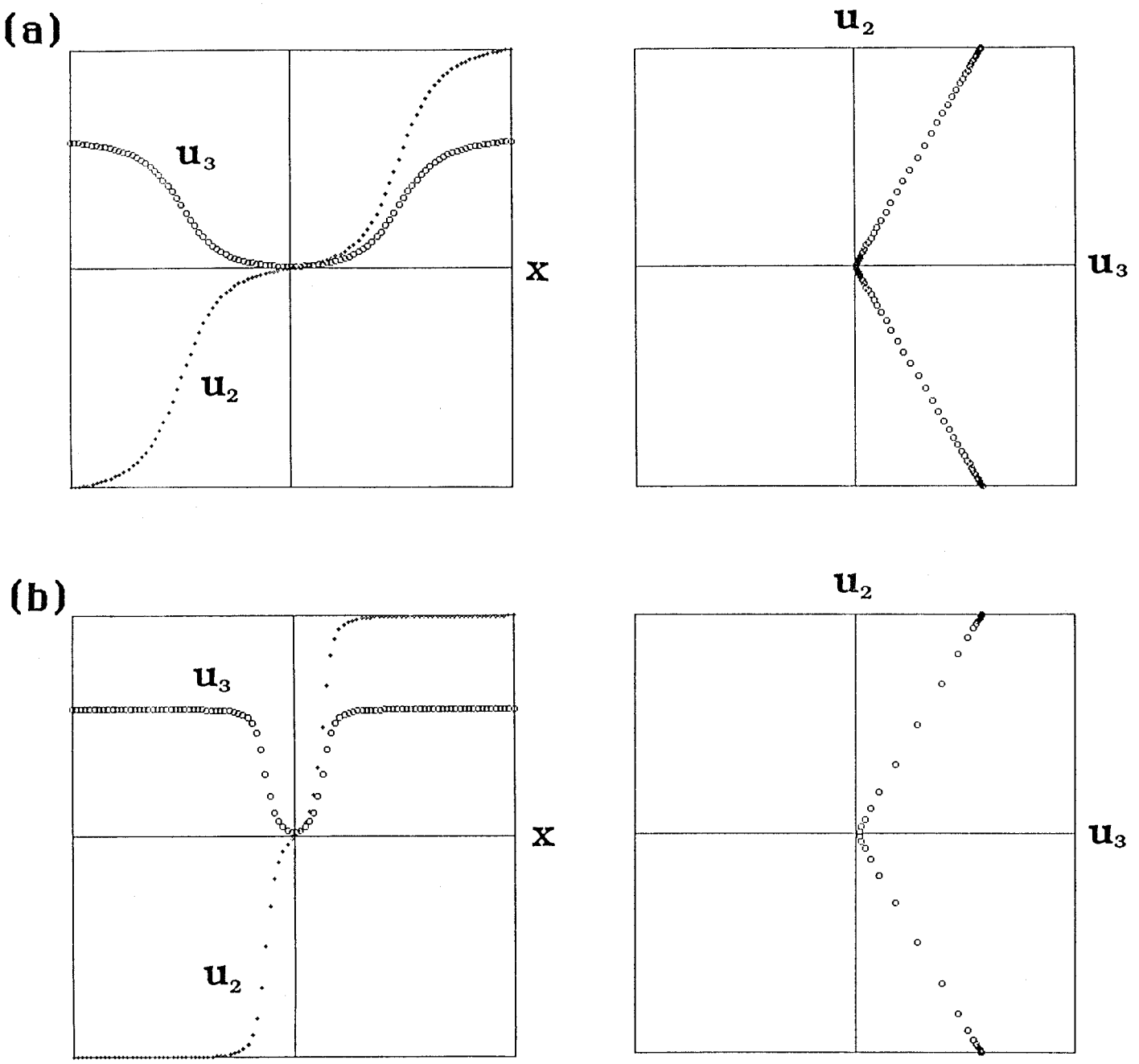

Fig.3-2 Typical examples of the results of calculations. The spatial variations of $u_2(x)$ and $u_3(x)$ are shown on the left side, and the trajectories of the system in (u_3,u_2) space when x is varied are shown on the right side. (a) For $T \sim T_c$. (τ=0.96, $\kappa/b=6.25\times10^{-6}$.) (b) For $T_0<T<T_c$. (τ=0.84, $\kappa/b=6.25\times10^{-6}$.)

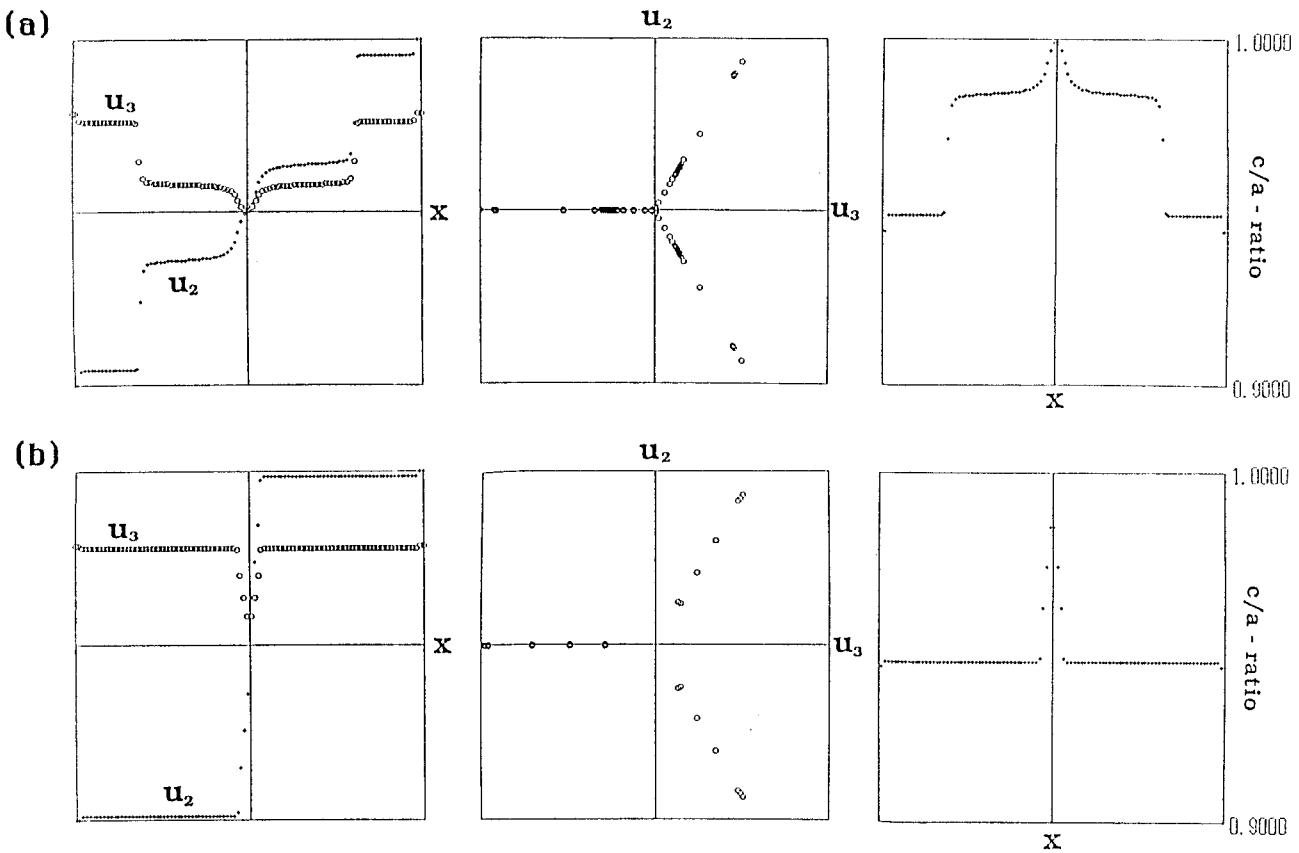

Fig.3-3 Typical examples of the results of calculations when the 5th- and 6th-order terms are taken into account in the potential function. In addition to the spatial variations of u_2 and u_3 (left) and the trajectories of the system (center), the spatial variation of c/a-ratios are given (right). (a) For $T_0<T<T_c$. (b) For $T<T_0$. Notice in (a), the system is practically expressed by a mixture of two tetragonal lattices. In (b), single tetragonal lattice is stabilized. Trajectories include the lines starting from different boundary conditions, so that they satisfy the threefold symmetry. (See the text.)

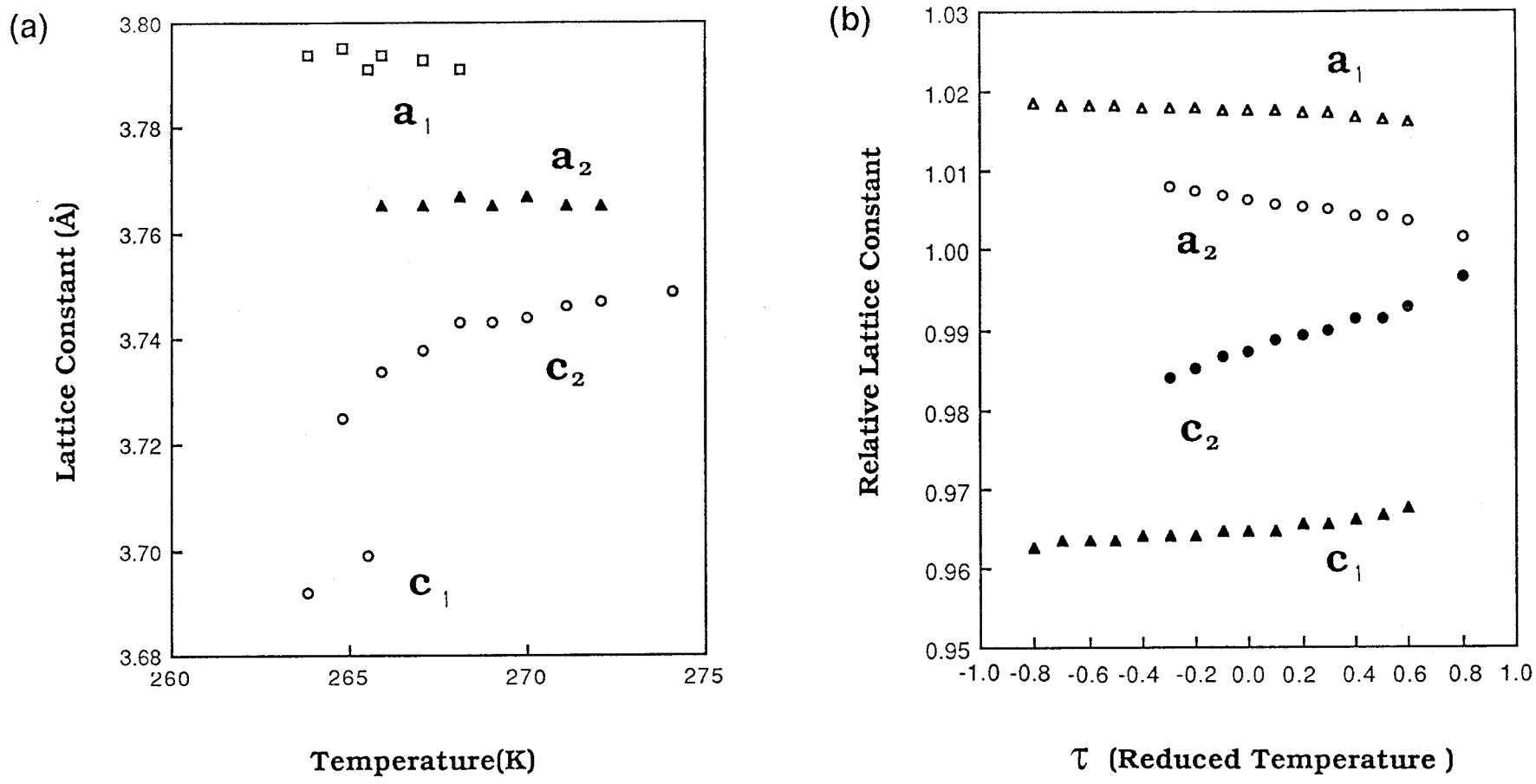

Fig.3-4 Temperature dependence of the lattice constants. (a) The same experimental results given in Fig.2-2-3(b). (b) The calculated lattice constants relative to the lattice constant in the cubic phase.

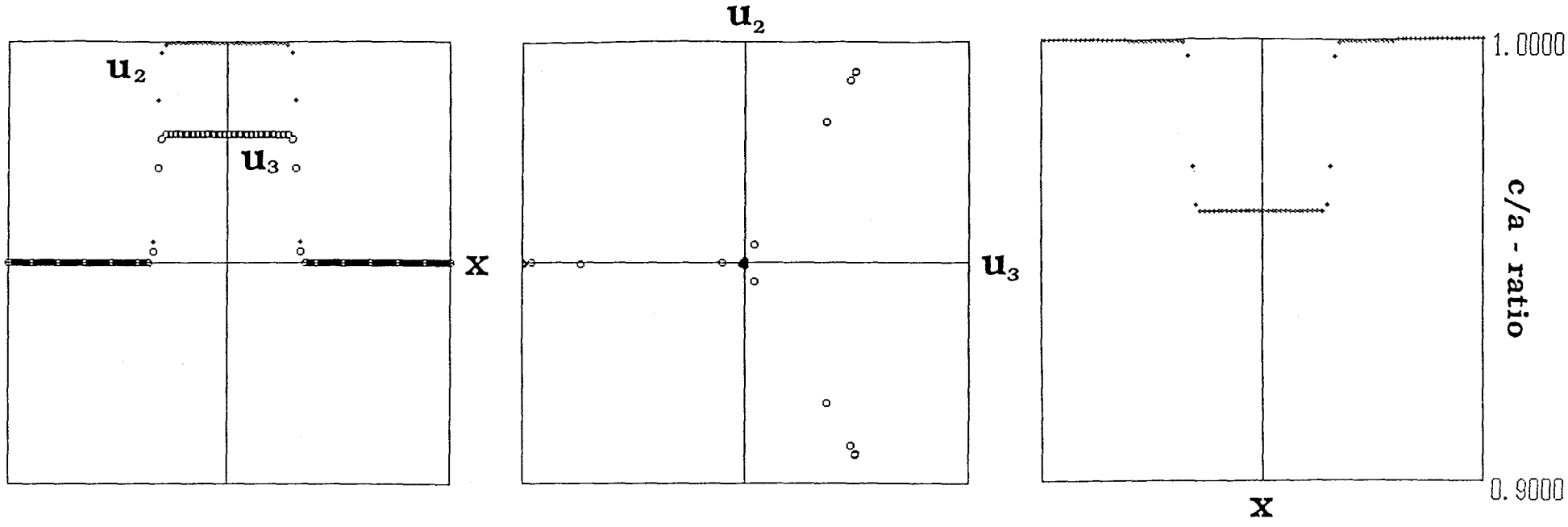

Fig.4-1 The spatial dependence of u_2 and u_3 (left), the trajectory (center) and the spatial variation of c/a-ratios (right) in regime (II) when the boundary condition (4-1) is imposed. This state corresponds to random distribution of 'embryos' within the parent cubic phase. (See the text.)

(a) (220)

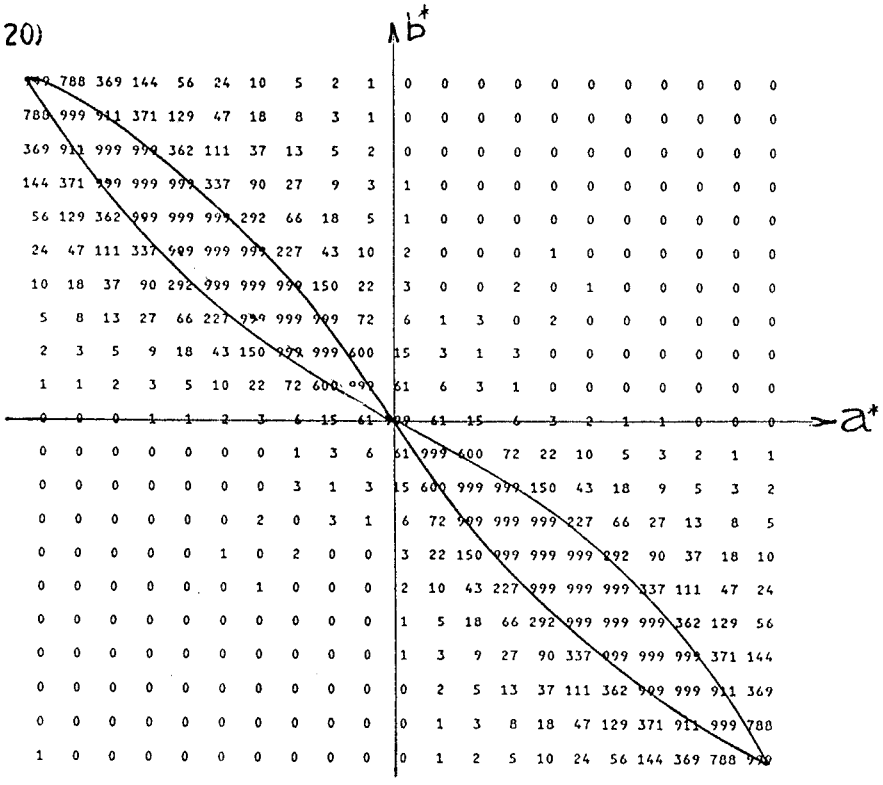

(b) (200)

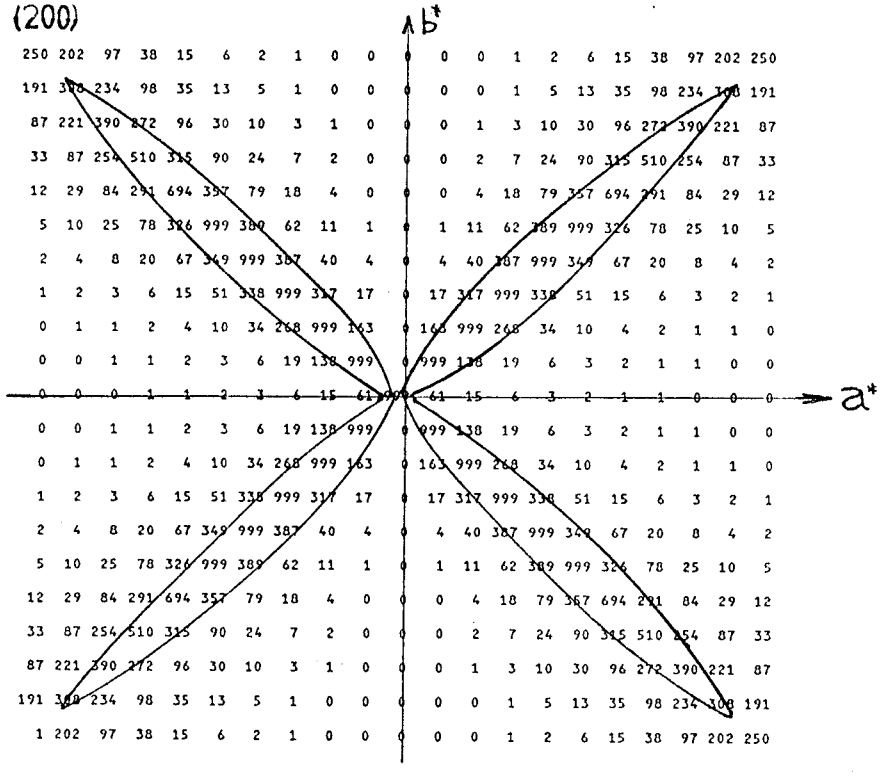

Fig.4-2 Calculated intensity contours of the Huang scattering around (a) (220) and (b) (200) Bragg points on the (hk0) plane when a 'tetragonal defect' exists in the cubic matrix. The horizontal and vertical axes indicate the a*-axis and the b*-axis, respectively.

(a) (220)

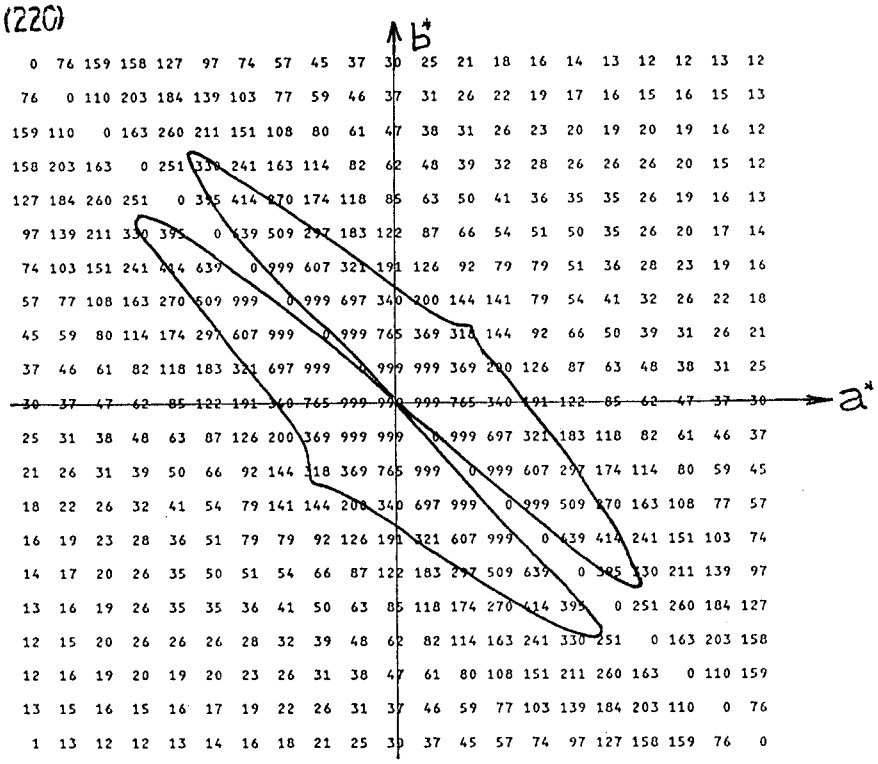

0	76	159	158	127	97	74	57	45	37	30	25	21	18	16	14	13	12	12	13	12
76	0	110	203	184	139	103	77	59	46	37	31	26	22	19	17	16	15	16	15	13
159	110	0	163	260	211	151	108	80	61	47	38	31	26	23	20	19	20	19	16	12
158	203	163	0	251	339	241	163	114	82	62	48	39	32	28	26	26	26	20	15	12
127	184	260	251	0	395	414	270	174	118	85	63	50	41	36	35	35	26	19	16	13
97	139	211	339	395	0	639	509	297	183	122	87	66	54	51	50	35	26	20	17	14
74	103	151	241	414	639	0	999	607	321	191	126	92	79	79	51	36	28	23	19	16
57	77	108	163	270	509	999	0	999	697	340	200	144	141	79	54	41	32	26	22	18
45	59	80	114	174	297	607	999	0	999	765	369	318	144	92	66	50	39	31	26	21
37	46	61	82	118	183	321	697	999	0	999	999	369	200	126	87	63	48	38	31	25
30	37	47	62	85	122	191	340	765	999	999	999	765	340	191	122	85	62	47	37	30
25	31	38	48	63	87	126	200	369	999	999	0	999	697	321	183	118	82	61	46	37
21	26	31	39	50	66	92	144	318	369	765	999	0	999	607	297	174	114	80	59	45
18	22	26	32	41	54	79	141	144	200	340	697	999	0	999	509	270	163	108	77	57
16	19	23	28	36	51	79	79	92	126	191	321	607	999	0	639	414	241	151	103	74
14	17	20	26	35	50	51	54	66	87	122	183	297	509	639	0	395	330	211	139	97
13	16	19	26	35	35	36	41	50	63	85	118	174	270	414	395	0	251	260	184	127
12	15	20	26	26	26	28	32	39	48	62	82	114	163	241	330	251	0	163	203	158
12	16	19	20	19	20	23	26	31	38	47	61	80	108	151	211	260	163	0	110	159
13	15	16	15	16	17	19	22	26	31	37	46	59	77	103	139	184	203	110	0	76
1	13	12	12	13	14	16	18	21	25	30	37	45	57	74	97	127	158	159	76	0

(b) (200)

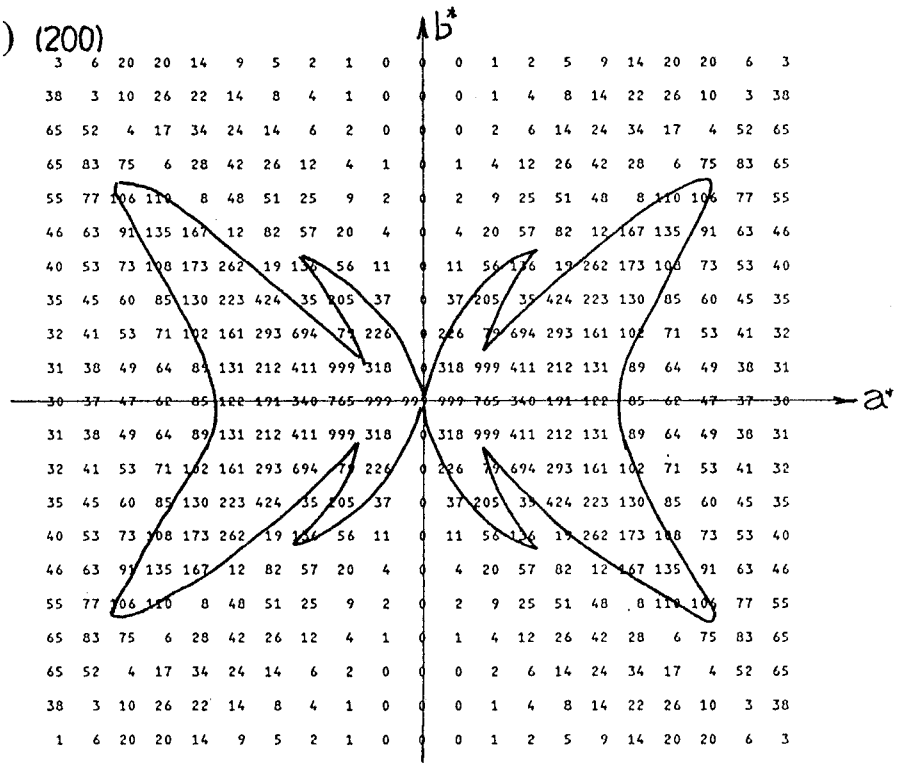

3	6	20	20	14	9	5	2	1	0	0	0	1	2	5	9	14	20	20	6	3
38	3	10	26	22	14	8	4	1	0	0	0	1	4	8	14	22	26	10	3	38
65	52	4	17	34	24	14	6	2	0	0	0	2	6	14	24	34	17	4	52	65
65	83	75	6	28	42	26	12	4	1	0	1	4	12	26	42	28	6	75	83	65
55	77	106	110	8	48	51	25	9	2	0	2	9	25	51	48	8	110	106	77	55
46	63	91	135	167	12	82	57	20	4	0	4	20	57	82	12	167	135	91	63	46
40	53	73	108	173	262	19	130	56	11	0	11	56	130	19	262	173	108	73	53	40
35	45	60	85	130	223	424	35	205	37	0	37	205	35	424	223	130	85	60	45	35
32	41	53	71	102	161	293	694	77	226	0	226	77	694	293	161	102	71	53	41	32
31	38	49	64	89	131	212	411	999	318	0	318	999	411	212	131	89	64	49	38	31
30	37	47	62	85	122	191	340	765	999	999	999	765	340	191	122	85	62	47	37	30
31	38	49	64	89	131	212	411	999	318	0	318	999	411	212	131	89	64	49	38	31
32	41	53	71	102	161	293	694	77	226	0	226	77	694	293	161	102	71	53	41	32
35	45	60	85	130	223	424	35	205	37	0	37	205	35	424	223	130	85	60	45	35
40	53	73	108	173	262	19	130	56	11	0	11	56	130	19	262	173	108	73	53	40
46	63	91	135	167	12	82	57	20	4	0	4	20	57	82	12	167	135	91	63	46
55	77	106	110	8	48	51	25	9	2	0	2	9	25	51	48	8	110	106	77	55
65	83	75	6	28	42	26	12	4	1	0	1	4	12	26	42	28	6	75	83	65
65	52	4	17	34	24	14	6	2	0	0	0	2	6	14	24	34	17	4	52	65
38	3	10	26	22	14	8	4	1	0	0	0	1	4	8	14	22	26	10	3	38
1	6	20	20	14	9	5	2	1	0	0	0	1	2	5	9	14	20	20	6	3

Fig.4-3 Calculated intensity contours of the Huang scattering around (a) (220) and (b) (200) Bragg points on the (hk0) plane for the case of 'isotropic defect'.

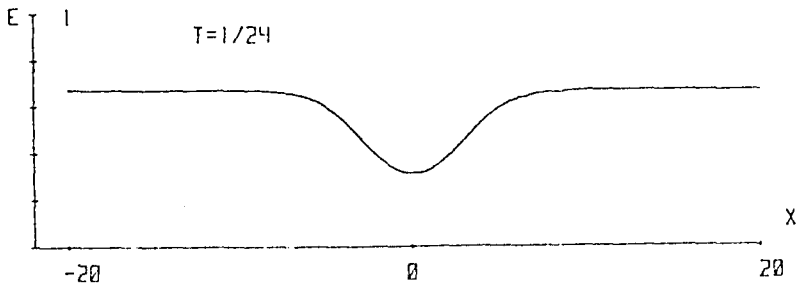

Fig.5-1 The structure of the soliton on martensite in an unbounded system. Although the temperature is higher than the transition temperature (T_c), major part of the system is the low temperature structure. (Fig.12 of ref.45.)

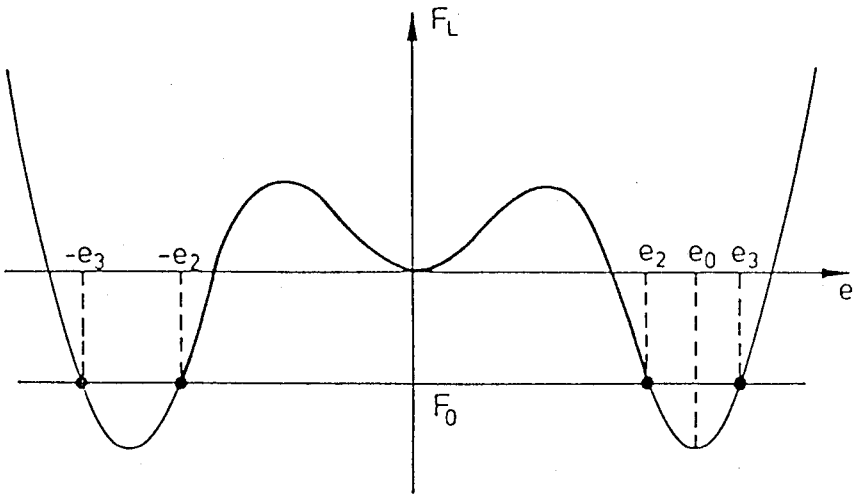

Fig.A-1 Potential curve of the system for the case of T<0 and F_0<0. The strain varies within the bold part of the curve. (Fig.3 of ref.45.)

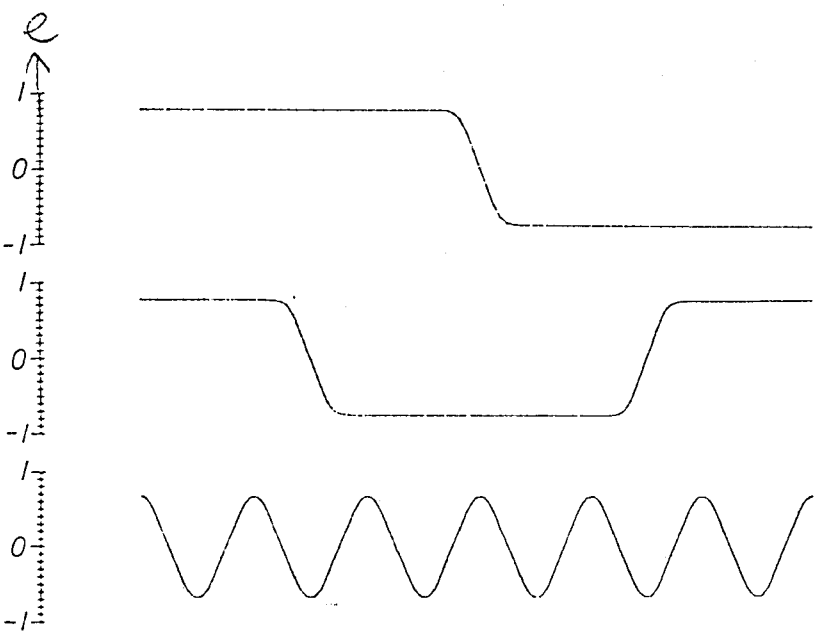

Fig.A-2 The structures of the solitons for T=-0.1 and $F_0 \approx F(e_0)$. The upper curve shows the structure of a single domain wall, the one in middle applies to double domain walls, and the lower one corresponds to the case of 12 domain walls. (Fig.5 of ref.45.)

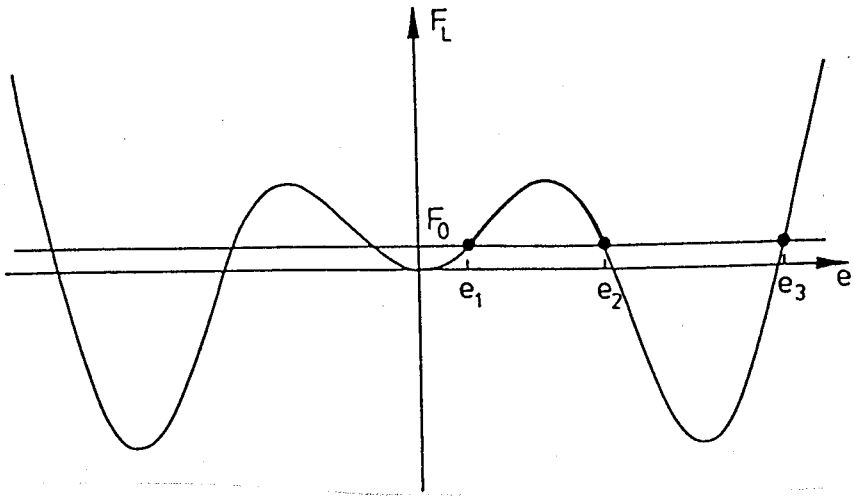

Fig.A-3 Potential curve for the case of $-1/4<T<0$ and $F_0>0$. (Fig.8 of ref.45.)

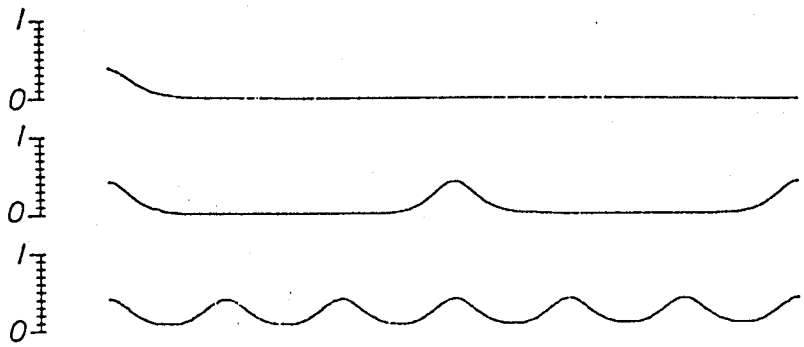

Fig.A-4 The soliton structures for $T=-0.1$ and $F_0>0$. They indicate the periodon solutions.(Fig.9 of ref.45.)